Investigating the Theoretical Feasibility of Longitudinal Motion Control in Indoor Cycling Trainers

By Jens A.N. Keijser

2023

Tu Delft and Tacx by Garmin
Master of Science – Thesis
Biomedical Engineering
Neuromusculoskeletal Biomechanics

Tacx A Garmin Company

TU Delft

"Investigating the Theoretical Feasibility of Longitudinal Motion Control in Indoor Cycling Trainers"

MSc Thesis Biomedical Engineering
Neuromusculoskeletal Biomechanics

by

Jens A.N. Keijser

Student number:	4980980	
Project date:	March 3, 2023	
Thesis committee:	dr. J.K. Moore	TU Delft
	prof. dr. H.E.J. Veeger	TU Delft
	Ir. J. Haasnoot	Tacx by Garmin

TU Delft

Abstract

As the indoor cycling trainer industry keeps innovating, a cycling trainer that has a similar longitudinal motion to outdoor cycling does not yet exist. Therefore, this thesis aimed to design a simulator controller that can actively simulate longitudinal cycling motion and assess its performance in translating outdoor longitudinal cycling dynamics to the indoor cycling trainer setup. Since the thesis concerned an indoor cycling setup the amount of allowed longitudinal motion was $\pm$ 20 cm.

We performed a literature review and motion study on the topic of longitudinal bicycling dynamics, whereafter equations of motion of outdoor cycling were defined to address the difference between in- and outdoor cycling. The gathered knowledge was then used to design a simulator controller for an indoor cycling setup that is actuated in the longitudinal direction through a linear actuator. To evaluate the performance of the simulator controller torque data of 4 different test subjects was collected and used as the input signal for the controller to theoretically assess its simulation performance.

The simulator controller simulations, of 7 different slope angles for both seated and standing cycling, resulted in minimal longitudinal motion of the simulated trainer setup during low-resistance cycling situations and maximal motion during high-resistance cycling situations. During the simulations, the simulated cycling trainer setup stayed well within the maximal allowable $\pm$ 20 cm from its initial position. The intra-pedal stroke range of motion of the simulations was similar to the intra-pedal stroke range of motion measured on a cycling treadmill through a motion capture study.

This thesis concludes that it is possible to translate outdoor longitudinal cycling dynamics to an indoor cycling simulator with torque as the only input. The theoretical assessment of the simulator controller shows that the metrics meet the requirements and are similar to real-world cycling.

Contents

Abstract ii

1 Introduction 1

2 Literature Review 5
2.1 Pedal Stroke . . . 5
2.2 Cyclist-Induced Forces . . . 7
2.3 Resistance Forces . . . 8
2.3.1 Aerodynamic Drag . . . 8
2.3.2 Gravitational resistance . . . 9
2.3.3 Rolling Resistance . . . 9
2.4 Bicycling Longitudinal Motion in Different Cycling Situations . . . 9

3 Real-World longitudinal Bicycle motion 11
3.1 Method . . . 11
3.1.1 Participants . . . 11
3.1.2 Equipment . . . 12
3.1.3 Protocol . . . 12
3.2 Results . . . 13

4 Equations of Motion 17
4.1 Propulsion force-based motion . . . 17
4.1.1 Outdoor cycling . . . 17
4.1.2 Indoor Cycling . . . 18
4.2 Non-Propulsion Force-Based Motion . . . 19
4.3 Differences Between Outdoor and Indoor Cycling . . . 20

5 Longitudinally Actuated Trainer Setup Concept 21

6 Simulator controller 24

7 Data collection method 29
7.1 Methods . . . 29
7.1.1 Participants . . . 29
7.1.2 Equipment . . . 30
7.1.3 Protocol . . . 31

8 Results 32

9 Discussion 41
9.1 Summary . . . 41
9.2 Interpretations . . . 41
9.3 Limitations . . . 43

10 Conclusion and Recommendations 45

A Appendix A - Treadmill Bicycle Acceleration 50

B Appendix B - Trainer Rolling Resistance Determination 54
B.1 Equipment . . . 54
B.2 Protocol . . . 54
B.3 Result . . . 54

List of Figures

1.1 An overview of the different types of indoor trainers (Tacx BV.) . . . 1
(a) Rollers, treadmill and stand-alone indoor trainers (from left to right) . . . 1
(b) Wheel-on and direct drive indoor turbo trainers . . . 1
1.2 An indoor cyclist using a smart turbo trainer to cycle in a virtual online world (Zwift) . . . 2
1.3 A LifeLine rockerplate and Tacx Motion Plates which are indoor cycling trainer accessories that allow passive longitudinal motion . . . 4

2.1 The coordinate system of the crank arm position. Where $theta$ resembles the rotation angle of the crank arm. . . . 5
2.2 A torque curve of one crank arm revolution for different cycling situations [16]. The data was gathered during an in the field test. Cycling on a level surface with a cadence of 100 rpm (L100), another level at 80 rpm (L80), a 9.25% incline at 80 rpm (U80), and a 9.25% incline at 60 rpm (U60). The experiments were executed at the same power output. . . . 6
2.3 Cyclist handlebar force in the longitudinal direction [20]. Three test subjects were measured during a 6% incline, seated cycling treadmill test. Cycling velocity was 7.2 m/s with a cadence of 84 rpm. . . . 7
2.4 Cylist and bicycle with propulsion force and resistance forces working on it . . . 8

3.1 The test subject is cycling on an inclined cycling treadmill to collect motion data of the bicycle. . . . 11
3.2 The markers for motion tracking on the rear wheel axis and seat stay to determine the longitudinal motion of the bicycle during treadmill cycling. . . . 13
3.3 The rear wheel marker displacement and crank torque for both cycling on a 0% and 15% inclined cycling treadmill. . . . 14
3.4 An illustration on how intra-pedal stroke range of motion is determined. The dataset is artificial for the sake of simplicity in understanding the concept. . . . 14
3.5 An illustration on how intra-pedal stroke range of motion is determined. The dataset is artificial for the sake of simplicity in understanding the concept. . . . 15
3.6 Bicycle rear wheel axis marker acceleration and the corresponding crank arm torque for 15% incline cycling treadmill riding. . . . 16

4.1 Free body diagrams of a bicycle and cyclist. Where all the relevant dimensions and forces are given that work on the bicycle and cyclist. **For the bicycle:** F_{d_b} is the aerodynamic drag force. F_{g_b} is the gravitational force. F_{rr} is rolling resistance force. F_{prop} is the propulsion force. F_{s_c}, F_{h_c}, and Fpc_x are the forces in the longitudinal direction by the cyclist on the saddle, handlebars, and pedals, respectively. F_c is the pedaling force perpendicular to the crank arm. D_w, D_c, and D_g are the diameters of the wheels, chainring, and cassette, respectively. L is the length of the crank arm. δ is the angular velocity of the rear wheel. θ is the angle of the crank arm. α is the angle of the slope ridden. **For the cyclist**: Fd_c is the aerodynamic drag resistance. Fg_c is the gravitational resistance. Fs_b, F_{h_b}, and F_{pb_x} are the forces from the saddle, handlebars, and pedals in the longitudinal direction, respectively. α defines the slope angle that is ridden. . . . 17
4.2 A schematic overview of a smart indoor trainer cycling setup. . . . 19
4.3 An illustration of a sprinters bicycle throw where internal forces cause motion. . . . 19
4.4 A free-body diagram of a bicycle throw. . . . 19

5.1 A conceptual idea of an actively controlled longitudinal moving indoor trainer setup. . . . 21
5.2 A free-body diagram of the concept active-controlled longitudinal motion trainer setup . 22

6.1 Block diagram of the longitudinal trainer motion simulator controller. The input variables are 1) Torque T_t measured by the smart indoor trainer around the axis of the flywheel which varies per timestamp (block 1). 2) The virtual slope angle $alpha$ communicated by the trainer every time stamp (block 1). 3) The mass of the cyclist, bicycle, and trainer which are set to a constant based on the cyclist. The simulator controller calculates the virtual sum of forces F_vir in block 3 and feeds that to the "Magic Equation" to determine the reference actuator force $F_{a_{ref}}$ (block 4). $F_{a_{ref}}$ is the reference signal for the actuator dynamics in block 5, where the mechanical and electromechanical losses are accounted for to determine the actual actuator force F_a. That actuator force actuates the trainer setup through block 6 which is an algebraic equation. The red outlined blocks resemble the plant in the simulator controller. 24
6.2 The calculated actuator reference force and its average value in the upper plot. The lower plot displays the detrended actuator reference force and its average value. The detrending was done with the Matlab function *sgolayfilt($F_{a_{ref}}$,1,$(2 \cdot Fs) + 1$)* 26
6.3 State description of the trainer setup, where x_t is the position of the trainer, $\dot{x}_t$ is the velocity of the trainer, and $\ddot{x}_t$ is the acceleration of the trainer. 27
6.4 The simulated position of the trainer setup without compensation for drift. The blue line is the position and the red line is the low-pass filtered trainer setup position to identify the drift. 27
6.5 The discrete PD controller that eliminates the drift of the trainer setup. 28
6.6 Drift compensated trainer setup position through the return-to-zero model. 28

7.1 The Tacx Neo 2T setup to collect torque data through a wireless Rasp connection. . . . 30
7.2 The wireless connection with the Tacx Neo 2T and Rasp through a Tacx custom-made antenna. 31

8.1 The torque input data for the simulator controller and the corresponding cadence for a slope of 0%. The color of the cadence curve indicates if the cyclist is in a seated or standing position or if she/he is in the transition phase between seated and standing cycling. 32
8.2 The torque input data for the simulator controller and the corresponding cadence for a slope of 25%. The color of the cadence curve indicates if the cyclist is in a seated or standing position or if she/he is in the transition phase between seated and standing cycling. 33
8.3 **Figure A** displays the mean virtual velocity per ridden virtual slope angle, where the solid lines resemble the seated cycling blocks and the dashed lines are the standing cycling blocks of the measurement. **Figure B** displays the virtual resistance force per virtual slope angle, where the solid lines resemble the seated cycling blocks and the dashed lines are the standing cycling blocks of the measurement. 34
8.4 The Peak torque values of all test subjects for different virtual inclines. The upper plot displays the seated block of the measurement whereas, the bottom plot displays the standing cycling peak torque values. 34
8.5 The simulation result of test subject 2, riding a 0% incline 35
8.6 The displacement of the bicycle measured on a 0% incline in the motion tracking study performed on a cycling treadmill for test subject 2. 36
8.7 The simulation result of test subject 2, riding a 25% incline 36
8.8 An overview of the intra-pedal cycling longitudinal range of motion of the simulated trainer setup for all the test subjects. The upper plot gives the range of motion for seated cycling per measured virtual slope angle. The bottom plot gives the range of motion for standing climbing for all measured virtual slope angles for all test subjects. 37

8.9 **Figure A** displays the peak torque for each test subject per slope angle, where the solid lines resemble the seated blocks and the dashed lines resemble the standing blocks of the data collection measurements. **Figure B** displays the cadence for each test subject per slope, where the solid lines resemble the seated blocks and the dashed lines resemble the standing blocks of the data collection measurements. **Figure C** displays the maximal positive and negative simulated actuator force for each slope angle for every test subject, where the solid lines resemble the seated blocks and the dashed lines resemble the standing blocks of the data collection measurements. **Figure D** displays the maximal and minimal simulated acceleration of the trainer setup per slope angle for each test subject. Where the solid lines resemble the positive acceleration and the dashed lines resemble the negative acceleration blocks of the data collection measurements. **Figure E** displays the simulated intra-pedal stroke range of motion per slope angle for each test subject, where the solid lines resemble the seated blocks and the dashed lines resemble the standing blocks of the data collection measurements. **Figure F** displays the maximal positive and negative simulated displacement of the trainer setup. Where the solid lines resemble the positive displacement and the dashed lines resemble the negative displacement blocks of the data collection measurements. 38
8.10 The virtual trainer setup acceleration and the measured torque curve for test subject 2 on a 15% virtual slope whilst cycling in the saddle. 39
8.11 The intra-pedal stroke range of motion for a motion capture study on a cycling treadmill, for the simulation of the trainer setup based on treadmill torque data, and for the average simulated intra-pedal stroke motion of the trainer setup based static trainer torque data. Note that the intra-pedal stroke range of motion is the displacement measurement of the bicycle, whereas the other simulations simulate the motion of the cyclist, bicycle, and trainer as one body. 40

9.1 The intra-pedal stroke range of motion for a motion capture study on a cycling treadmill, for the simulation of the trainer setup based on treadmill torque data, and for the average simulated intra-pedal stroke motion of the trainer setup based static trainer torque data. Note that the intra-pedal stroke range of motion is the displacement measurement of the bicycle, whereas the other simulations simulate the motion of the cyclist, bicycle, and trainer as one body. 42

A.1 Bicycle rear wheel axis marker acceleration and the corresponding crank arm torque for 0% incline cycling treadmill riding. 50
A.2 Bicycle rear wheel axis marker acceleration and the corresponding crank arm torque for 2.5% incline cycling treadmill riding. 51
A.3 Bicycle rear wheel axis marker acceleration and the corresponding crank arm torque for 5% incline cycling treadmill riding. 51
A.4 Bicycle rear wheel axis marker acceleration and the corresponding crank arm torque for 7.5% incline cycling treadmill riding. 52
A.5 Bicycle rear wheel axis marker acceleration and the corresponding crank arm torque for 10% incline cycling treadmill riding. 52
A.6 Bicycle rear wheel axis marker acceleration and the corresponding crank arm torque for 12.5% incline cycling treadmill riding. 53
A.7 Bicycle rear wheel axis marker acceleration and the corresponding crank arm torque for 15% incline cycling treadmill riding. 53

List of Tables

3.1 An overview of the average intra-pedal stroke longitudinal bicycle motion for riding a cycling treadmill with inclines from 0% to 15%. The values are for the one measured test subject. 15

7.1 The characteristics of the test subjects that participated in the data collection experiments. 29

8.1 Am overview of test subject 1 for all ridden virtual slope angles of the measured torque peaks for seated and standing cycling, the seated and standing cadence rpm, and the average power per block of seated and standing cycling. 33
8.2 The simulation results of test subject 2 for different slope angles (0% to 25%). F_a is the actuator force in N. $\ddot{x}_t$ is the acceleration of the trainer setup. IPS RoM is the intra-pedal stroke range of motion and is divided into the seated and standing parts of the simulation. x_t is the position of the trainer setup. 37
8.3 The peak torque around the rear wheel for treadmill cycling and static smart trainer cycling for various measured (virtual) inclines. Both peak torque values are measured during seated cycling. 39
8.4 The difference between intra-pedal stroke range of motion between simulations with treadmill and static trainer acquired torque data, expressed as a percentage of treadmill intra-pedal stroke range of motion measured in treadmill cycling through a motion study. 40

1

Introduction

Since the COVID-19 pandemic loomed in 2019, the number of road cyclists increased significantly in most western cities and the cycling population will most likely not shrink in the coming years [1]. Consequently, indoor cycling has also grown in the last couple of years.

Indoor cycling can act as a substitute for outdoor cycling when the weather is too bad or if the sun has set early during winter time. Indoor cycling, therefore, makes it possible to keep training and maintain (cycling) fitness [2], [3].

The main users of indoor cycling trainers are road race cyclists, however, the trainers are also suited for mountain bikers, gravel bikers, track cyclists, and even hand bikers. This means that an indoor cycling trainer can act as a substitute for all cycling disciplines.

There are different indoor cycling trainers that have different properties; indoor trainers to which a bicycle (or part of it) must be connected, as well as standalone indoor trainers. Figure 1.1 gives an overview of the trainers mentioned.

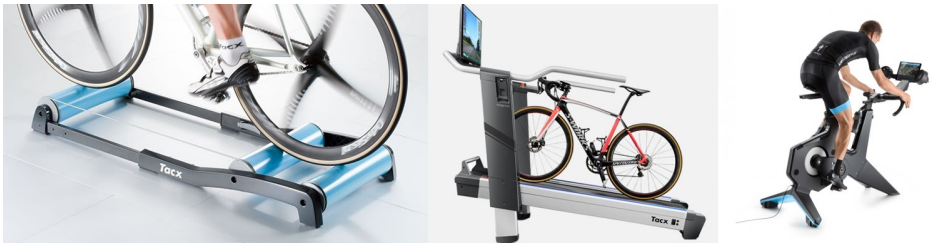

(a) Rollers, treadmill and stand-alone indoor trainers (from left to right)

(b) Wheel-on and direct drive indoor turbo trainers

Figure (1.1) An overview of the different types of indoor trainers (Tacx BV.)

Indoor trainers that require a bicycle to use are; rollers, treadmills, and turbo trainers. A roller consists of three cylindrical rolls that are attached to a rectangular frame. There are two rollers in the back of the roller trainer on which the rear wheel of the bicycle rests. When pedaling, the rear wheel of the bicycle spins these rolls. The front wheel of the bicycle rests on top of the front roller. The front roller is connected to the middle roller with a snare to allow the front roller to spin as well. The front roller must

spin to stabilize the bicycle. The level of resistance rollers trainers offer cannot be adjusted. Roller trainers are mainly used for warming up because they are convenient to bring to a race for instance and the bicycle does not have to be dismounted to use the roller trainers.

A cycling treadmill works the same way as a treadmill that is used for running. The speed of the belt can be increased or decreased, as well as the angle to mimic a slope for uphill cycling. A cycling treadmill allows for the same motion of the bicycle as on a road, which makes it the most realistic trainer in comparison to outdoor cycling.

A turbo trainer is a static stand that is clamped to the rear of a bicycle and can produce a constant or varying resistance. Resistance is produced by turbines in the earliest models (hence turbo trainer), flywheels, fluid discs, or magnets. There are two types of turbo trainers, wheel-on and direct drive turbo trainers. A wheel-on turbo trainer presses the rear tire of the bicycle on a drum which transfers the resistance of the trainer. A direct drive turbo trainer acts as a replacement rear wheel, meaning that the resistance is transferred to the bicycle by the cassette.

A stand-alone indoor cycling trainer does not require a bicycle to function as it is basically a static bicycle. A stand-alone trainer produces resistance the same way that turbo trainers do.

Figure (1.2) An indoor cyclist using a smart turbo trainer to cycle in a virtual online world (Zwift)

Most cyclists own so-called smart indoor trainers, these trainers are controlled by a computer. The smart trainers are able to simulate resistances as they would in outdoor cycling. These resistances are gravitation resistance, rolling resistance, and aerodynamic drag resistance. If one of these virtual resistances changes, the cyclist will realize that the real-world resistance torque that the trainer delivers to the drivetrain of the bicycle will increase. The resistances change as the virtual cycling course or virtual cycling velocity changes. The smart trainer also measures the torque the cyclist produces around the axis of the trainer. Based on that torque and the virtual resistance forces virtual velocity is calculated by the smart trainer.

Smart indoor cycling trainers can be connected to applications that enable cyclists to ride in virtual worlds. Virtual online training has become popular in the last couple of years [4]. Virtual online training allows an indoor cyclist to cycle in an online virtual world, through an application such as Zwift, where physical performance on the indoor trainer is translated into a cycling action of an online avatar [5]. This makes indoor training more engaging and allows cyclists to organize online meetups and even races, without the need to leave their houses.

The main advantages of a cycling indoor trainer are that: 1. regardless of the outdoor weather conditions one can continue training which is beneficial to the (cycling) fitness. 2. There is no interaction with other road users that can cause dangerous situations. 3. Interval training can be done precisely because the outside-world variables, like traffic lights and corners, are not present. 4. It can save time compared to outdoor cycling. 5. The bicycle used does need less frequent cleaning. 6. Hill climbing resistance can be simulated if you live in a flat area. These 6 properties make indoor cycling a convenient and safe substitute for outdoor cycling.

Of course, indoor cycling trainers do have disadvantages. Trainers can be costly, especially when used as an addition to an already-owned bicycle. Indoor trainers do not improve bicycle handling skills as they are static and no maneuvers are required. As the indoor cycling system is often rigid, except for some play, the cyclist experiences non variable pressure points that can lead to discomfort in the hands and the seat area. The effectiveness of cycling on an indoor trainer is still under debate as the rigidness of the trainer might have an influence on the muscles used in comparison to outdoor cycling [2]. The static nature of an indoor cycling trainer will not fully substitute the outdoor cycling experience because of the lack of motion.

The motion differences between cycling indoors and outdoors can also lead to a difference in training effect. Muscle activity patterns vary between indoor- and outdoor cycling [2]. Some muscles have increased activity up to 17%, whereas the activity of other muscles decreased by 19% compared to cycling outdoors. The static properties of an indoor cycling setup are therefore responsible for a change in cycling technique [2]. When using an indoor trainer as a substitute for outdoor cycling training, the same muscle activity, and technique are desirable. This is important to achieve the optimal cycling training effect.

Motion of a bicycle also plays a part in the comfort experienced by a cyclist. Prolonged pressure on a single part of the body can cause numbness and discomfort [6]–[9]. Bicycle motion is assumed to distribute pressure on the saddle in time and therefore relieve pressure points, hence a more comfortable cycling experience. The bicycle movement also relieves pressure points on the hands, preventing numbness [6]. Participants of a test with a static trainer and a cycling treadmill state that an indoor trainer feels less smooth and therefore unpleasant [2]. Therefore, a non-static indoor trainer is assumed to be more comfortable than a static trainer.

The indoor cycling branch aims to create the most immersive indoor cycling experience for their consumers. Smart trainers make it possible to ride in (realistic) virtual worlds that contribute to an immersive cycling experience. There are also accessories available that enable the steering and pitching of the bicycle to mimic the virtual slope.

Figure (1.3) A LifeLine rockerplate and Tacx Motion Plates which are indoor cycling trainer accessories that allow passive longitudinal motion

Other accessories allow motion that is caused by the cyclists' behavior. Examples are rocker plates and Tacx Motion Plates Figure 1.3. The rocker plate is a construction of two plates with dampers and/or springs in between them. When a cyclist moves on the bicycle the plate will rock in that direction. The Tacx Motion Plates are an accessory that is placed underneath the trainer. Within the Motion Plates, wheels make it possible for the trainer to move in the longitudinal direction. The motion is a result of the forces that a cyclist exerts on the bicycle it is on.
The mentioned accessories allow for motion in indoor cycling trainer setups, however, the motion is controlled passively. Although the motion contributes to the comfort and experience of the user, its pattern is not as realistic as outdoor cycling. As stated before, motion differences between outdoor cycling and static cycling lead to different cycling techniques. The same is assumed for a different motion pattern between an indoor trainer and outdoor cycling.

The goal of indoor cycling trainer manufacturers is to provide the most comfortable and immersive cycling experience possible, without compromising the performance and training effect of the users. In order to achieve that goal the motion of indoor cycling must follow the same movement pattern as an outdoor bicycle would.

The goal of this thesis is to design a realistic motion simulator controller for indoor cycling trainers. Riding a bicycle is a complex dynamic system [10]–[12]. Capturing all the dynamics of a bicycle is too extensive for this thesis. Therefore, only longitudinal motion will be accounted for. However, indoor cycling trainer setups are used indoors where space is a limiting factor. Therefore, this space limitation must be accounted for in the simulator design. The simulator controller will be designed for actively controlled motion of the trainer setup. Actively controlled means that a computer controls the motion electromechanically. Since smart trainers measure the torque around the axis of the flywheel, which is the only variable from which a force can be derived, torque must be the input signal for the simulator controller. Hence the following research equation.

"What is the theoretical performance of a controller translating outdoor longitudinal cycling dynamics to an indoor simulator setup with torque as the only input signal?"

The coming chapters of this thesis will discuss longitudinal bicycle dynamics, the equations of motion of indoor and outdoor cycling and their differences, a conceptual trainer setup for which the simulator controller is designed, the simulator controller, the data collection method, and the results of the longitudinal cycling motion simulator controller simulations for different test subjects.

2

Literature Review

Since this thesis will determine the dynamics for a longitudinal motion simulator controller, it is key to getting a better understanding of the dynamics that cause that motion in outdoor cycling. Therefore, outdoor road cycling dynamics will be discussed in the coming section.

The forces that act on a bicycle and cyclist can be divided into two categories: Cyclist-induced forces and resistance forces. The cyclist-induced forces are forces that are exerted on the pedals, handlebar, and saddle of the bicycle. The resistance forces are gravitational force, aerodynamic drag, and rolling resistance.

2.1. Pedal Stroke

A cyclist propels his bicycle by exerting force on the pedal perpendicular to the crank arm [13], [14]. This force is transmitted to the rear wheel via the drive chain of the bicycle, where it becomes the propulsion force. The force perpendicular to the crankarm is called the effective force.

A complete pedal stroke is made when the crank arms have turned 360°around the rotation axis. Figure 2.1 shows the coordinate system of a crank arm. θ resembles the rotation angle of the crank arm.

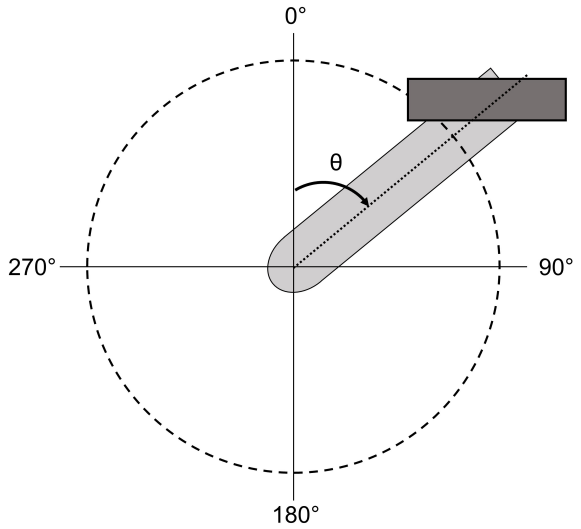

Figure (2.1) The coordinate system of the crank arm position. Where $theta$ resembles the rotation angle of the crank arm.

The effective force is responsible for the torque [Nm] a cyclist produces around the crank since torque is the product of the crank arm length [m] and the effective force [N]. To calculate the power [W] a cyclist produced torque is multiplied by the angular velocity of the crank arm [rad/s] [15].

The torque curve is a sinusoidal function in which the values depend on the crank angle and the cycling situation [15], [16]. At around 90°angle of the crank arm, the torque is found to be at its peak value, whereas minimal values are around 180 °of the crank arm angle (Figure 2.2) [16].

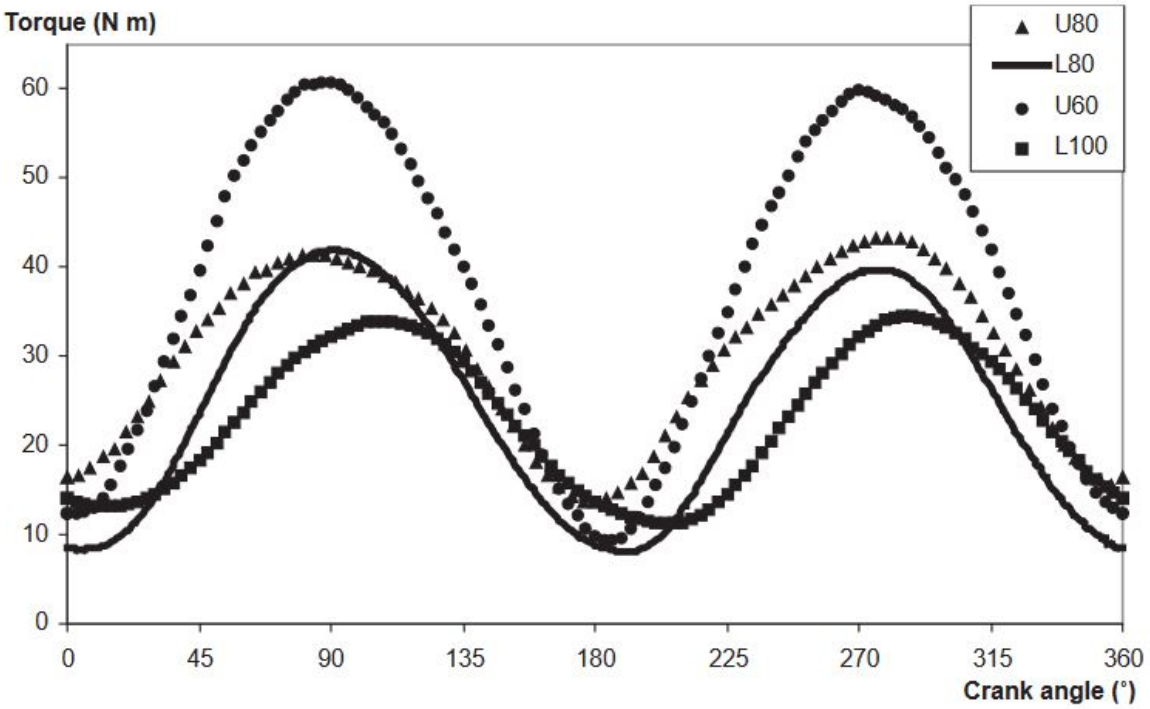

Figure (2.2) A torque curve of one crank arm revolution for different cycling situations [16]. The data was gathered during an in the field test. Cycling on a level surface with a cadence of 100 rpm (L100), another level at 80 rpm (L80), a 9.25% incline at 80 rpm (U80), and a 9.25% incline at 60 rpm (U60). The experiments were executed at the same power output.

As shown in Figure 2.2 the form of the torque curve depends on the cycling situation. In the experiments by Bertucci et al., cyclists were asked to cycle with varying cadences and incline on the same power output for all experiments [16]. It is clear that the lower the cadence is, the higher the torque becomes. This is no surprise since the power is a function of the angular velocity of the crank arm and the torque.

However, when closely comparing the uphill cycling at 80 rpm (U80) and level cycling at 80 rpm (L80), a difference can be seen in the torque curve. For uphill cycling, the torque starts to increase earlier in the pedal stroke compared to level cycling. This may be the result of a difference in the cycling position during uphill cycling. However, it can also be caused by less inertial crank load since inertial crank load depends on cadence and gear ratio which are lower during uphill cycling as we will discuss in Equation 2.2.

Inertial load can be defined as:

$$T = I \cdot \ddot{\theta} \tag{2.1}$$

Where I is the moment of inertia and $\ddot{\theta}$ is the anglular acceleration of the crank arms. Crank inertial load for a bicycle is then defined as the following equation [17]:

$$\left[I_F + \left(\frac{R_F}{R_G} \right)^2 (R_D^2(m_B + m_C + 2m_D + m_F + m_G) + (2I_D + I_G)) \right] \ddot{\theta} \tag{2.2}$$

Where I_F is the rotational inertia sum of the crank arms, chainrings, and pedals. $\frac{R_F}{R_G}$ is the gear ratio. R_D is the radius of a bicycle wheel. m_B, m_C, m_D, m_G are the masses of the bicycle frame, cyclist, wheels, and the freehub. m_F is the sum of the mass of the crank arms, chainrings, and pedals. I_D is is the rotational inertia of a wheel and I_G the rotational inertia of the freehub. $\ddot{\theta}$ is the angular acceleration

of the crank arm around its spinning axis. Note that the part between square brackets is the inertia of the spinning parts and the effective inertia of the linear moving parts of the bicycle.

As seen in Equation 2.2 the crank inertial load is a function of the gear ratio and cadence. Decreasing the gear ratio, thus shifting to an easier gear, leads to less inertial crank load for the same cadence. Lowering the cadence also decreases the inertial crank load.

Low inertial crank load makes a cyclist will have to apply more torque to achieve the same power output compared to cycling with high inertial crank load. When cycling resistance increases a cyclist is forced to change gear ratio and/or cadence in order to keep cycling. Because of this adaptation crank inertial load will decrease as well which will lead to a different cyclist-produced torque curve compared to high inertial crank load cycling.

Thus, based on the resistance a cyclist has to overcome the crank inertial load changes and consequently does the torque curve. This tells us that high resistance cycling will lead to greater and prolonged torque compared to low resistance cycling where a cyclist can maintain a high gear ratio and high cadence.

2.2. Cyclist-Induced Forces

A cyclist also applies force on the pedal that is not perpendicular to the crank arm and, therefore, will not contribute to the propulsion force at the rear wheel. However, the longitudinal fraction of that force might contribute significantly to the longitudinal motion of the bicycle and must not be neglected.

A cyclist exerts forces on the handlebars of the bicycle as well. The cyclist does this to amplify the power output [18]. These forces affect the longitudinal motion of the bicycle. Studies by Stone and Hull (1993 & 1995) have shown that forces from -116N to 90N are exerted in the handlebar in the longitudinal direction [19], [20]. These forces were measured during standing cycling on a treadmill (8% slope, 73 RPM). The -116N force was measured at 124°of the pedal stroke, where 0°is the vertical position of the clockwise turning crank arm. The force of 90N was exerted at 337°of the upward pedal stroke. Hence, during one pedal stroke a pulling force is present during the down stroke and a pushing force during the upstroke.

The same force pattern is seen in seated cycling on a treadmill (6% slope, 84 RPM) (Figure 2.3) [20]. However, the forces are lower and the moment in the pedal stroke has shifted. The maximum force measured is 40N at 320°of the pedal stroke, whereas the minimal force on the handlebars is -75N at 60°. Despite the differences in force, the studies tell us that cyclists apply force on the handlebars. These forces may well result in a motion of the bicycle and, therefore, must be taken into account when designing the simulator controller .

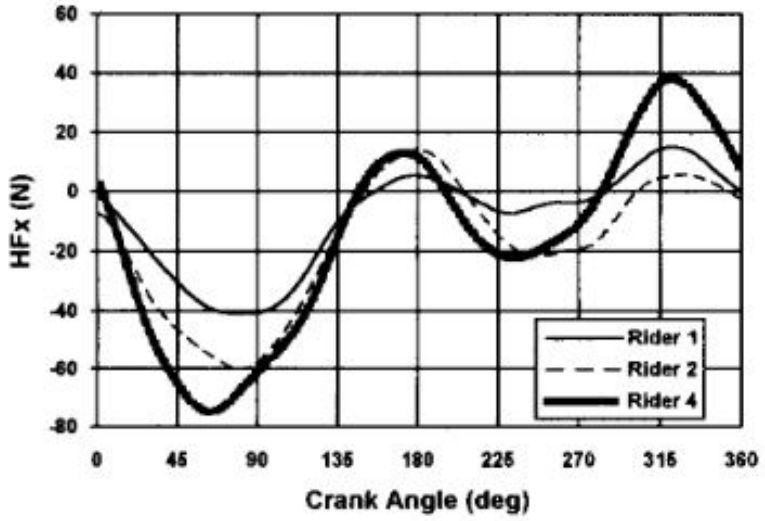

Figure (2.3) Cyclist handlebar force in the longitudinal direction [20]. Three test subjects were measured during a 6% incline, seated cycling treadmill test. Cycling velocity was 7.2 m/s with a cadence of 84 rpm.

Since a cyclist sits on the saddle for most of the time whilst riding, loads are applied on the saddle. These loads can also lead bicycle motion in the longitudinal direction. Literature on the topic of saddle loads, states that forces on the saddle in the longitudinal direction are up to 12% percent of the cyclist's body weight [21], [22]. The peak of this force occurs at 61°of the pedal stroke and is in the forward direction.

2.3. Resistance Forces

A cyclist must match the propulsion force to the resistance forces to maintain velocity. To accelerate the propulsion force must be greater than the sum of the resistance forces. The resistance forces that work on the cyclist and bicycle are aerodynamic drag, gravitational resistance, and rolling resistance Figure 2.4. Note that gravity and aerodynamic drag acts on the bicycle and the cyclist. Whereas rolling resistance only works on the bicycle.

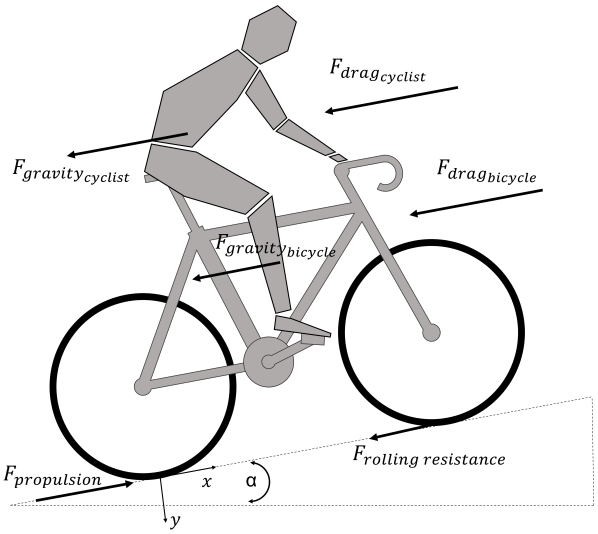

Figure (2.4) Cylist and bicycle with propulsion force and resistance forces working on it

In the following section it will be discussed how these resistance forces may influence the longitudinal motion of the bicycle and cyclist.

2.3.1. Aerodynamic Drag

Aerodynamic drag is often the greatest resistance a cyclist needs to overcome. When cycling at speeds of $14\ m/s$ and higher, aerodynamic drag is responsible for 90% or more of the total resistance acting on the bicycle and cyclist system [23]–[26]. At lower speeds, the aerodynamic drag is much less dominant because the aerodynamic drag force (F_{drag}) is proportional to the squared velocity:

$$F_{drag} = \frac{1}{2} \cdot \rho \cdot C_d \cdot A \cdot sgn(v)v^2 \tag{2.3}$$

Where $\rho\ [kgm^{-}3]$ is the density of the air, $A\ [m^2]$ the frontal surface area of the cycling system, $v\ [m/s]$ velocity with respect to the wind velocity. $sgn(v)$ places the sign of v before the v^2 to ensure the force works in the right direction. C_d is a dimensionless drag coefficient [27]. C_d is often combined with A as a single variable. C_dA depends on the surface texture, size, and shape of the bicycle and cyclist. Altering the cycling position can, therefore, have a significant effect on the C_dA value and consequently on aerodynamic drag [28]–[30].

In indoor cycling, there is no aerodynamic drag present, since, the cyclist and bicycle do not move. Therefore, the drag is calculated based on the virtual velocity that a smart indoor trainer determines. Whereafter, the aerodynamic drag is applied as a counter torque in the trainer. In that way, the cyclist will experience more resistance at higher virtual velocities.

2.3.2. Gravitational resistance

When cycling up or down an angled surface gravity applies a force on the bicycle and cyclist. The size of the force is dependent on the mass of the cyclist and bicycle as well as the angle of the slope (α in Figure 2.4). The gravitational resistance works in the longitudinal direction and is described as Equation 2.4:

$$F_g = (m_{cyclist} + m_{bicycle}) \cdot g \cdot sin(\alpha) \tag{2.4}$$

Where $m_{cyclist}$ and $m_{bicycle}$ are the mass of the cyclist and bicycle respectively. g is the gravitational constant if $9.81\ m/s^2$. Note that gravitational resistance, unlike aerodynamic drag, is not dependent on velocity. If the ridden slope becomes a descent, the direction of the gravitational force will flip and, therefore, work in the cycling direction instead of the opposite.

In outdoor cycling gravity 'pulls' the cyclist back. However, in indoor cycling, this is not the case since it is done on a level surface and is static. Just like aerodynamic drag, the gravitational resistance is calculated by the smart indoor trainer and then applied as a counter torque.

2.3.3. Rolling Resistance

Rolling resistance is the amount of energy lost due to tire deformation during cycling since rubber is a viscoelastic material. Viscoelastic means that energy is lost while a material deforms and then reforms to its initial form [25], [31]. The rolling resistance force (F_{rr}) is defined as Equation 2.5:

$$F_{rr} = C_{rr} \cdot m \cdot g \cdot cos(\alpha) \tag{2.5}$$

Where C_{rr} is the rolling resistance coefficient and is unitless, m is the mass of the system, g is the gravitational constant. $cos(\alpha)$ takes account for the slope that is ridden, with α being the slope angle. A steeper slope leads to less rolling resistance since the mass has less influence.

Typical values of the C_{rr} for cycling smooth asphalt lies around 0.004, however, coarse gravel C_{rr} can be 0.018 [25]. This tells us that, rolling resistance is also dependent on the surface structure ridden.

Rolling resistance is normally the smallest resistance that works on the bicycle. Still, the force may not be neglected, since it affects the longitudinal motion of a bicycle. Unlike drag and gravity, it does not exert force on the cyclist himself.

An indoor trainer must calculate the virtual rolling resistance based on a predefined C_{rr} value since this force is also absent in indoor cycling.

The three resistance forces explained in the previous part are very large and, therefore, an important part of real-world cycling dynamics. In order to design a simulator controller that can realistically simulate longitudinal cycling motion in an indoor setup, the resistance forces must be included in the dynamics of that simulator controller.

2.4. Bicycling Longitudinal Motion in Different Cycling Situations

There are different cycling situations in which cyclists may find themselves. The situations in this thesis are defined as easy to hard cycling and as seated and standing cycling. During easy cycling situations such as riding a level surface, cadence and gear ratio are high as well as the velocity. Since the cadence is high, torque is lower for the same power output with a lower cadence, power is the product of cadence and torque.

There is a difference between seated and standing cycling. Cyclists adopt a lower cadence when cycling out of the saddle for the same power output [32]. When cycling with a lower cadence the bicycle has more team in between torque peaks to decelerate before it gets propelled again. The torque is higher as well for low cadence cycling at the same power, meaning that the bicycle will accelerate more per pedal stroke. It can, therefore, be assumed that the longitudinal motion of the bicycle is larger whilst cycling out of the saddle for the same power output since the cadence is lower.

To conclude, in cycling situations where cadence and velocity are high and torque is low, the longitudinal change in motion of the bicycle will be minimal. Whereas, when cadence and velocity are low and torque is high the longitudinal change in cycling motion will be maximal.

A high cadence is larger than 120 rpm and a low cadence is lower than 60 rpm [33], [34]. Whereas optimal cycling cadence is stated to be 80 - 100 rpm [35], [36]. For torque, it is more complicated to define what value of torque is high. Since bicycle acceleration is a function of mass and torque it is better to look at torque per kilogram. However, it is obvious that more torque leads to more acceleration and, thus giving exact values to low and high torque is not necessary.

Previously discussed topics of chapter 2 all contribute to the longitudinal dynamics of the bicycle. However, from the literature, it has not become clear how exactly the combination of the longitudinal bicycling dynamic contributors affects the bicycle motion and therefore, what is realistic longitudinal bicycling motion. To get a more complete understanding of the longitudinal bicycling motion, more knowledge must be gained. In order to gain that knowledge a longitudinal cycling motion study will be performed in the coming chapter 3.

3

Real-World longitudinal Bicycle motion

The goal of this thesis is to design a simulator controller to simulate longitudinal motion in an indoor cycling trainer setup and assess its performance. Due to time constraints, no physical setup will be built. Therefore, the simulator controller must be validated theoretically. To assess the simulator controller we must compare the behavior of the simulator controller to real-world cycling.

To obtain a better understanding of how a road bicycle moves in the longitudinal direction a structured motion capture study was conducted on a cycling treadmill, the Tacx Magnum. During this study, the longitudinal motion of the bicycle was measured for different incline angles of the treadmill. Figure 3.1 shows the setup of the Tacx Magnum that is used to collect the motion data of the bicycle.

Figure (3.1) The test subject is cycling on an inclined cycling treadmill to collect motion data of the bicycle.

3.1. Method

In this section, the method of the motion capture study to determine the longitudinal motion for different slope angles will be described.

3.1.1. Participants

For this motion-tracking study, only one participant was measured. The participant was a well-trained 27-year male who weighed 91 kg and was 1.95 m tall. Only one test subject was measured because cycling at a constant velocity is hard on this specific treadmill. The Tacx Magnum is a smart treadmill that controls its belt speed based on the cyclist's position. If the cyclist moves forward the belt will

increase velocity, whereas if the cyclist moves backward the belt will decrease velocity. Only a 30 cm area allows the belt to maintain velocity. It took the test subject a significant amount of practice to stay within the constant belt velocity margin. Therefore, it was decided to only measure with one test subject.

3.1.2. Equipment

The data were collected with the following equipment:

1. A road bicycle with 50/34 chainrings and 11 to 34 sprocket cassette.
2. Garmin Rally power pedals (Garmin, Olathe, Kansas, USA)
3. A Tacx Magnum cycling treadmill (Tacx by Garmin, Oegstgeest, Netherlands).
4. The Tacx Training App (Tacx by Garmin, Oegstsgeest, Netherlands).
5. Rasp Tacx device data collection software (Tacx by Garmin, Oegstsgeest, Netherlands).
6. ANT+ antenna (Tacx by Garmin, Oegstsgeest, Netherlands).
7. A GoPro HERO 10 camera (GoPro, San Mateo, California, USA).
8. Kinovea 0.9.5 video analyzing software (Free Software Foundation, Boston, Massachusetts, USA).
9. Matlab (Mathworks, Natick, Massachusetts, USA).
10. Markers.
11. Camera tripod.

The road bicycle that was used for the test is a standard modern road bicycle with common gearing to ensure the bicycle resembles a normal outdoor bicycle. The bicycle was equipped with Garmin Rally power pedals to measure left and right crank torque.

The Tacx Magnum cycling treadmill can be controlled through the Tacx Training App to which pre-made workouts can be uploaded which can vary in slope. A variation in slope in the workout results in a variation of the treadmill slope as well. The treadmill can adopt slopes from 0% to 15%. During the measurement data from the Tacx Magnum is extracted through Rasp with a sampling frequency of 64 Hz.

The GoPro camera was used to film the marker at the axis of the rear wheel and the seat stay of the bicycle. The markers are 5 cm diameter circle with a small white dot in the middle to have a high contrast point in the marker. The high contrast results in better motion tracking performance by Kinovea.

Kinovea is a motion analyzing software primarily for sports. Coordinate systems can be made in the software to acquire motion data of tracked markers.

3.1.3. Protocol

The protocol for this experiment consists of cycling the treadmill for different slope angles. The inlines were 0% to 15% with increments of 2.5%. A slope workout was made in the Tacx Training App which increased the slope angle every 2 minutes. Connection with Rasp was made to extract belt velocity and slope angle data from the treadmill.

Markers were applied to the axis of the rear wheel and the seat stay with a 10 cm center-to-center gap between each other. The seat stay marker was not tracked but was used in combination with the axis marker to define the coordinate system in Kinovea. The camera was placed close to the rear wheel to gain optimal tracking performance of the marker as is shown in Figure 3.2.

Figure (3.2) The markers for motion tracking on the rear wheel axis and seat stay to determine the longitudinal motion of the bicycle during treadmill cycling.

The stepwise protocol is as follows:

1. Connection to the treadmill was made through the Tacx Training App.
2. The camera was turned on just as the power pedals. A synchronization point was made by tapping the cranks 3 times on film.
3. The test subject took place on the treadmill with the bicycle and started the workout.
4. During all slope angles the cyclist tried to reach steady-state cycling as soon as possible with a suited gear ratio for the cycling situation. The gear ratio was noted per slope.
5. After the measurement the torque data were extracted from the pedals through the ANT+ antenna and loaded into Matlab.
6. The video of the measurement was loaded into Kinovea where a coordinate system was defined and the rear axis marker was tracked for the duration of the measurement. Thereafter, the position data of the marker was loaded into Matlab.
7. The belt speed and slope angle data acquired through Rasp were also loaded into Matlab.
8. In Matlab the torque data and treadmill data were resampled to the sampling frequency of the video, which was 30 Hz. This was done through the Matlab function *interp1*.
9. The video data and torque data were cut at the synchronization point made in step 2.
10. Thereafter the velocity of the treadmill and cadence-based velocity were synchronized using the Matlab function *ginput*.
11. After the previous steps the measurement data was ready to process, which was done in Matlab.

3.2. Results

This section gives the main results of the motion tracking study performed. The goal was to obtain a better understanding of how a bicycle moves in a longitudinal direction while cycling in the real-world.

The most important metric is the marker displacement during the tests. Figure 3.3 displays the marker displacement of cycling on a 0% slope and on a 15% slope. The crank torque produced by the cyclist is also plotted in the figure to get an understanding of how the torque increases as the slope becomes steeper.

We clearly see that the motion of the marker on the 15% incline has the same frequency as the cadence since it has the same frequency as the crank torque. For 0% incline cycling, this can be seen in the figure as well but is less convincing.

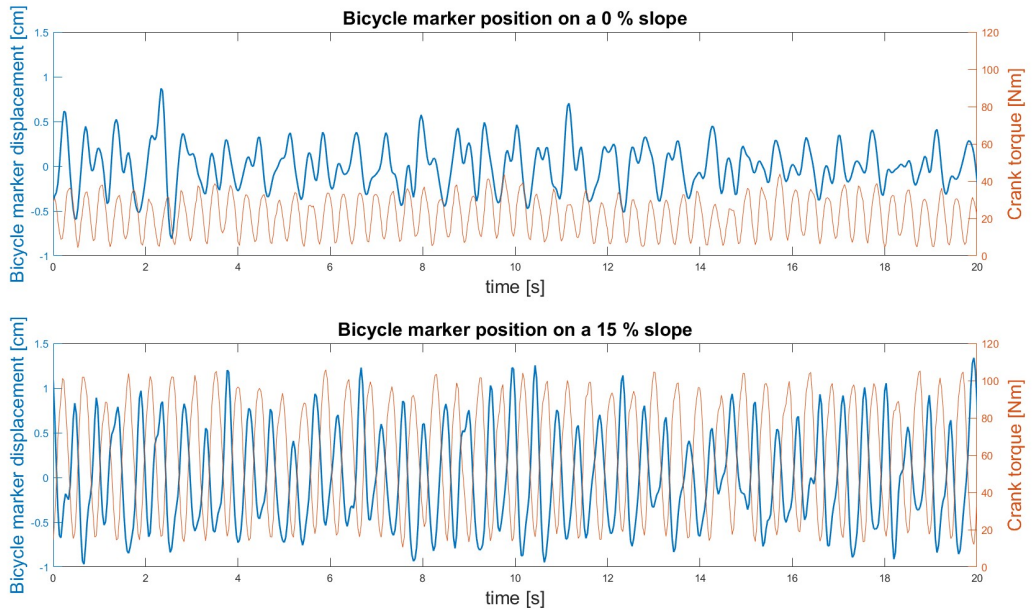

Figure (3.3) The rear wheel marker displacement and crank torque for both cycling on a 0% and 15% inclined cycling treadmill.

Furthermore, we observe that the motion in 0% climbing is less than for the 15% slope angle. To compare the difference numerically the term intra-pedal stroke range of motion is invented. This metric quantifies the amount of longitudinal motion within one pedal stroke. and is calculated by determining the magnitude of the vertical distance from a motion peak to the next valley as is illustrated in Figure 3.4 where an artificial dataset has been used to simplify the concept.

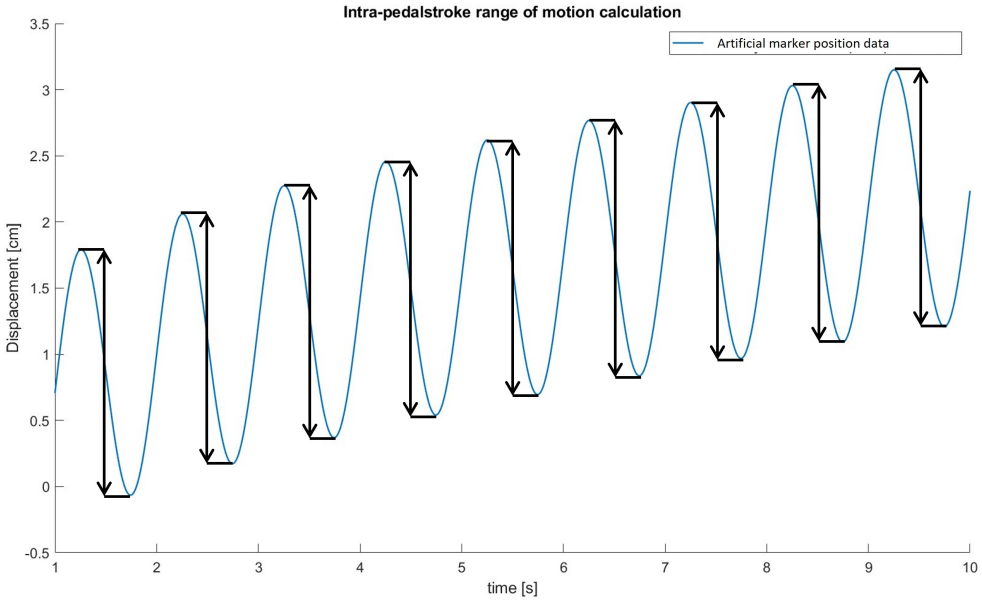

Figure (3.4) An illustration on how intra-pedal stroke range of motion is determined. The dataset is artificial for the sake of simplicity in understanding the concept.

Table 3.1 gives an overview of the average intra-pedal stroke range of motion of the marker for all slope angles ridden by the only test subject. The table tells us that the intra-pedal stroke range of motion increases as the slope angle becomes steeper.

Table (3.1) An overview of the average intra-pedal stroke longitudinal bicycle motion for riding a cycling treadmill with inclines from 0% to 15%. The values are for the one measured test subject.

Magnum incline percentage	0%	2.5%	5%	7.5%	10%	12.5%	15%
Intra-pedal stroke range of motion [cm]	0.514	0.542	0.638	0.634	0.771	1.113	1.276

In Figure 3.5 the intra-pedal stroke range of motion is displayed as a curve to show the rate at which the intra-pedal stroke range of motion increases per slope angle. It stands out from 5% to 7.5% there is a small decrease present. The rate at which the range of motion increases is also higher from 7.5% to 15% compared to the less steep slope angles.

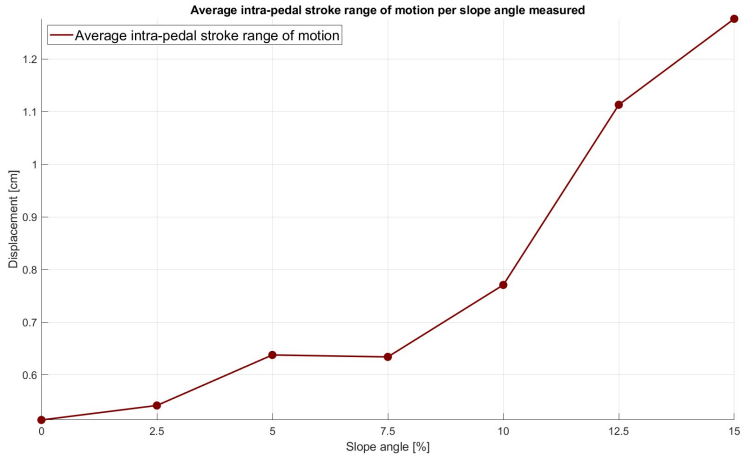

Figure (3.5) An illustration on how intra-pedal stroke range of motion is determined. The dataset is artificial for the sake of simplicity in understanding the concept.

When we observe the acceleration of the bicycle and the crank arm torque corresponding to it for riding a 15% incline on the cycling treadmill, it stands out that the acceleration curve of the bicycle does not match the shape of the torque curve (Figure 3.6). There is a clear notch in the acceleration curve where the crank arm torque peaks. This notch is also present in the data sets for the shallower incline angles, however, decreases in prominence as the incline becomes less steep. The marker accelerations of the other slope angles are displayed in Appendix A. The marker acceleration was calculated by differentiating the marker position twice.

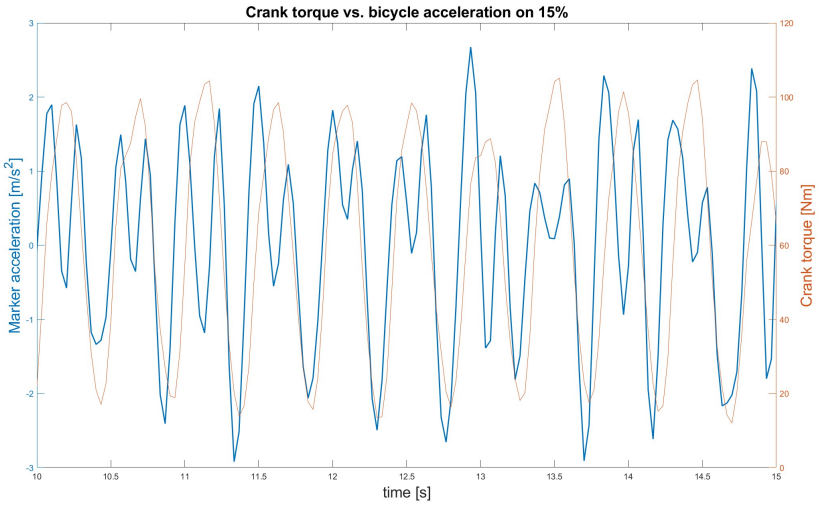

Figure (3.6) Bicycle rear wheel axis marker acceleration and the corresponding crank arm torque for 15% incline cycling treadmill riding.

When taking the formula for acceleration based on force and mass in mind:

$$a_b = \frac{F_b}{m_b + m_c} \tag{3.1}$$

Where a_b is the bicycle acceleration. F_b is the sum of forces working on the bicycle and cyclist, consisting of the propulsion force, gravitational force, and rolling resistance. m_b and m_c are the mass of the bicycle and cyclist respectively.

The resistance forces are constants since they only depend on the slope angle which is constant in this case. However, if the resistance force is constant, the acceleration curve must have the same shape as the crank arm torque curve since propulsion force is a function of that torque solely. Therefore, there must be another force active in the system that causes the notch in the acceleration curve. This force must be a sum force that is applied to the bicycle by the cyclist himself. When addressing Figure 2.3 it shows that there is a peak handlebar force present in the backward direction at a 45°to 90°crank arm angle. This is during the same pedal stroke phase as where peak crank arm torque is produced.

Based on the motion capture study and literature we assume that the cyclist pulls his handlebars during the pedal stroke to amplify the torque in hard cycling situations such as climbing a steep incline as done in this experiment. The interaction between the cyclist and the bicycle is, therefore, very important to keep into account whilst designing a longitudinal cycling motion simulator controller.

It is also found that the phase of the crank arm torque and the bicycle acceleration is coincides for all of the ridden inclines. This is not surprising since bicycle acceleration is a direct result of crank arm torque.

4

Equations of Motion

Since the forces that act on the bicycle and cyclist are known it is helpful to create free-body diagrams to gain further insight into how the forces exactly cause the motion of the cyclist and bicycle in an outdoor and indoor cycling scenario. Chapter 3 will elaborate in detail on the free-body diagrams and the motion equations derived from them.

4.1. Propulsion force-based motion

A bicycle is driven forward by the propulsion force and withheld by the resistance forces. The sum of these forces is the main determinant of cycling velocity. In this section, the forces and corresponding equations of motion that lead to the propulsion of the bicycle will be discussed.

4.1.1. Outdoor cycling

First, the equations of motion of the outdoor cycling system will be discussed in detail. Figure 4.1 displays a free-body diagram of a bicycle and a cyclist riding in a generic outdoor cycling situation.

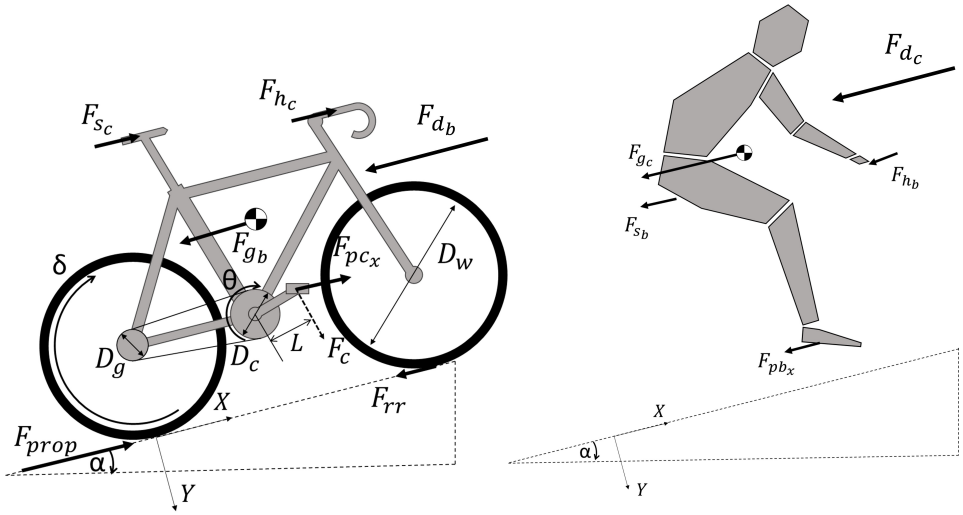

Figure (4.1) Free body diagrams of a bicycle and cyclist. Where all the relevant dimensions and forces are given that work on the bicycle and cyclist. **For the bicycle:** F_{d_b} is the aerodynamic drag force. F_{g_b} is the gravitational force. F_{rr} is rolling resistance force. F_{prop} is the propulsion force. F_{s_c}, F_{h_c}, and Fpc_x are the forces in the longitudinal direction by the cyclist on the saddle, handlebars, and pedals, respectively. F_c is the pedaling force perpendicular to the crank arm. D_w, D_c, and D_g are the diameters of the wheels, chainring, and cassette, respectively. L is the length of the crank arm. δ is the angular velocity of the rear wheel. θ is the angle of the crank arm. α is the angle of the slope ridden. **For the cyclist**: Fd_c is the aerodynamic drag resistance. Fg_c is the gravitational resistance. Fs_b, F_{h_b}, and F_{pb_x} are the forces from the saddle, handlebars, and pedals in the longitudinal direction, respectively. α defines the slope angle that is ridden.

There are three force types exerted on the bicycle 1, Forces that the cyclist directly applies. 2, the resistance forces. 3, the propulsion force. The three forces in the longitudinal direction on the bicycle

that the cyclist directly applies: F_{sc} (saddle force), F_{hc} (handlebar force), and F_{pc_x} (pedal force). F_p stands for the propulsion force and is a result of F_c which is the force perpendicular to the crank arm. That force is then transmitted through the drivetrain to the rear wheel. F_c can only work in the clockwise direction of the crank arm since the free hub of a bicycle does not engage in the other direction. The resulting forces are resistances: F_{rr} is the rolling resistance and F_{gb} is the gravitational resistance. Where three force types work on the bicycle, only two work on the cyclist. Contact forces from the bicycle and resistance forces. F_{sb} is a force at the saddle, F_{hb} is a force at the handlebars and F_{pb_x} is the at the pedals in the longitudinal direction.

The resistance forces that work on the cyclist are gravitational resistance (F_{gc}) and aerodynamic drag (F_{dc}). Note that rolling resistance is only exerting force on the bicycle and not on the cyclist, therefore, only two resistance forces act on the cyclist. Whereas, three work on the bicycle.

With the insights gained from the free-body diagrams, equations of motion were derived to define the longitudinal motion behavior of the cyclist and bicycle as a result of the forces acting on them (Equation 4.1 and Equation 4.6).

$$\sum F_{Bicycle} : F_{sc} + F_{hc} + F_{pc_x} + F_{prop} - F_{gb} - F_{rr} - F_{db} = m_b \cdot a_b \tag{4.1}$$

F_{prop} is a function of the gear ratio, the crank arm length L, and F_c.

$$F_{prop} = F_c \left(\frac{G_r}{G_f} \right) \left(\frac{L}{\frac{D_w}{2}} \right) \tag{4.2}$$

Where G_r and G_f are the numbers of teeth on the front and rear gear on which the chain engages. Shifting gears will lead to a change in propulsion force as F_c remains constant.

F_{gb} and F_{rr} both depend on the slope angle α and the mass of the bicycle and/or cyclist.

$$F_{gb} = g \cdot m_b \cdot sin(\alpha) \tag{4.3}$$

$$F_{rr} = C_{rr} \cdot g \cdot (m_b + m_c) \cdot cos(\alpha) \tag{4.4}$$

Aerodynamic drag resistance on the bicycle depends on the C_dA value and velocity of the bicycle, C_{d_b}, A_b, and v_b in Equation 4.5.

$$F_{db} = \frac{1}{2} \cdot \rho \cdot C_{d_b} \cdot A_b \cdot v_b^2 \tag{4.5}$$

The equation of motion of the longitudinal motion of the cyclist is defined as followed (Equation 4.6).

$$\sum F_{Cyclist} : -F_{sb} - F_{hb} - F_{pbx} - F_{gc} - F_{dc} = m_c \cdot a_c \tag{4.6}$$

Where F_{gc} now depends on the mass of the cyclist instead of the bicycle. The aerodynamic drag force F_{dc} depends on the C_dA value and velocity of the cyclist.

4.1.2. Indoor Cycling

The equations of motion given in the previous section give an insight into how a bicycle will move in an unconstrained outdoor cycling scenario. However, this thesis focuses on implementing realistic longitudinal motion simulation in an indoor cycling trainer setup. To obtain a clear understanding of where the differences lie between indoor and outdoor cycling.

The current indoor cycling setup with the use of a smart indoor trainer is shown schematically in Figure 4.2. The system contains three bodies, the trainer, the bicycle, and the cyclist **??**. The trainer is attached to the bicycle in the same way a rear wheel would be. The chain of the bicycle transfers the effective force to the cassette that is mounted on the trainer. Here the force makes the flywheel of the trainer spin.

Figure (4.2) A schematic overview of a smart indoor trainer cycling setup.

Indoor cycling trainers are designed in such a way that they do not move whilst cycling on one. cycling trainers are, therefore, technically fixed to the ground. Hence, the absence of equations of motion for this section.

4.2. Non-Propulsion Force-Based Motion

As mentioned before the main driving force of a bicycle is the propulsion force at the rear wheel. However, internal forces can also affect longitudinal motion. In that case conservation of momentum applies to the system, meaning the center of mass of the bicycle and cyclist maintain the same velocity but the separate centers of mass can change velocity.

An example of a non-propulsion force-based motion is a sprinters bicycle throw as illustrated in Figure 4.3. In a bicycle throw a cyclist pushes the bicycle forward with respect to himself. This is done to gain an advantage over his competition having the front wheel cross the finish line first. After the throw, the cyclist pulls the bicycle back to the initial cycling position.

Figure (4.3) An illustration of a sprinters bicycle throw where internal forces cause motion.

A free-body diagram of the bicycle throw scenario is displayed in Figure 4.4.

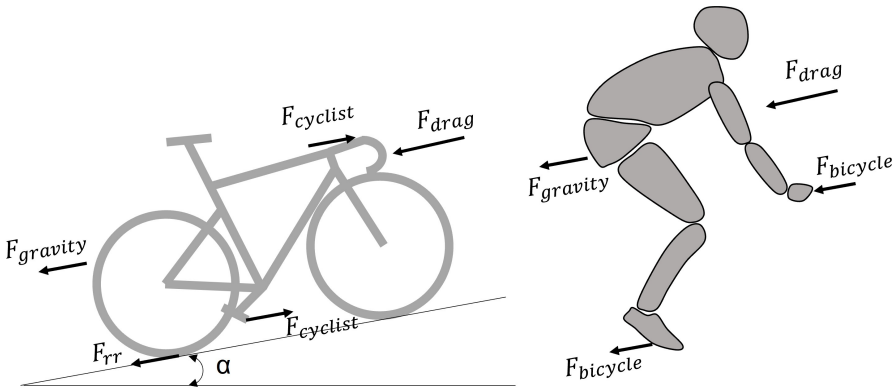

Figure (4.4) A free-body diagram of a bicycle throw.

If we want to describe the motion between the cyclist and bicycle with respect to each other we must look in the non-inertial frame where the bicycle moves with respect to the cyclist. Because the frame is non-inertial since the cyclist does not have a constant velocity, the external forces are left out of the equation.

We know that conservation of momentum applies to the interaction between the bicycle and the cyclist. Therefore, the following equation applies as well:

$$v_{b1} \cdot m_b + v_{c1} \cdot m_c = v_{b1} \cdot m_b + v_{c1} \cdot m_c \tag{4.7}$$

Where v_{b1} and v_{c1} are the velocities of the bicycle and cyclist before interaction occurs. v_{b2} and v_{c2} are the velocities of the bicycle and cyclist before interaction occurs. m_b and m_c are the masses of the bicycle and cyclist, respectively.

Conservation of momentum comes from Newonton's first law, which states that every action has an equal and opposite reaction. Therefore, the force applied by the cyclist on the bicycle results in an equal opposite reaction force from the bicycle:

$$F_{cyclist} = -F_{bicycle} \tag{4.8}$$

Which is equal to:

$$m_c \cdot a_c = -(m_b \cdot a_b) \tag{4.9}$$

Where a_c and a_b are the acceleration of the cyclist and bicycle, respectively. Hence, the acceleration of the cyclist and bicycle equations for the non-inertial frame:

$$a_c = \frac{-(m_b \cdot a_b)}{m_c} \tag{4.10}$$

$$a_b = \frac{(m_c \cdot a_c)}{-m_b} \tag{4.11}$$

It is clear that the actions of the cyclist can cause motion of the bicycle while conserving the momentum of the bicycle and the cyclist. This motion can affect the position of the trainer when simulation longitudinal cycling dynamics. Therefore, the internal cycling forces must not be neglected in designing the longitudinal motion simulator controller.

4.3. Differences Between Outdoor and Indoor Cycling

Since this thesis will focus on designing a simulator controller that can simulate realistic outdoor longitudinal motion in an indoor trainer, it is important to have a clear understanding of the differences between indoor and outdoor cycling. In the previous subsection 4.1.1 & subsection 4.1.2 the motion of outdoor cycling and the absence of motion in indoor cycling were discussed.

The cyclist-induced forces on the saddle, handlebars, and pedals are present in both indoor and outdoor cycling. However, these forces in an indoor cycling setup, as it is now, will not lead to motion of the bicycle in the longitudinal direction as the indoor cycling trainer constrains the motion. In outdoor cycling, there are three resistance forces working on the bicycle and cyclist, whereas in indoor cycling there are zero. However, the trainer produces a resistance torque based on the calculated resistance that is seen as the resistance. The torque is the result of an internal force and, therefore, will not lead to motion. Propulsion force is also absent in an indoor setup since the chain spins the flywheel of the trainer. This, again, is an internal force in the system and will not cause motion.

It is clear that the indoor cycling trainer contains the bicycle from moving in the longitudinal direction. Therefore, outdoor present propulsion and resistance forces are absent in indoor cycling. To realistically simulate longitudinal bicycle motion in an indoor training setup it, obviously, needs a degree of freedom over its longitudinal axis. The absent forces that cause longitudinal motion outdoors must also be produced in an indoor cycling setup. A conceptual idea on how to do this will be discussed in chapter 5.

5

Longitudinally Actuated Trainer Setup Concept

The goal of this thesis is to design an active longitudinal motion simulator controller to simulate realistic longitudinal motion in an indoor cycling trainer setup. In chapter 5 a concept will be discussed which could be controlled. This concept must be able to move in the longitudinal direction and apply substitute outdoor cycling forces.

The idea is to use a linear actuator to apply the sum of the missing forces to a free-to-move indoor cycling trainer. A concept trainer setup is shown in Figure 5.1. A linear actuator is fixed to a non-moving base. The piston is attached to the indoor trainer which is on wheels that make it able to roll. The front wheel is able to freely roll in the longitudinal direction as well.

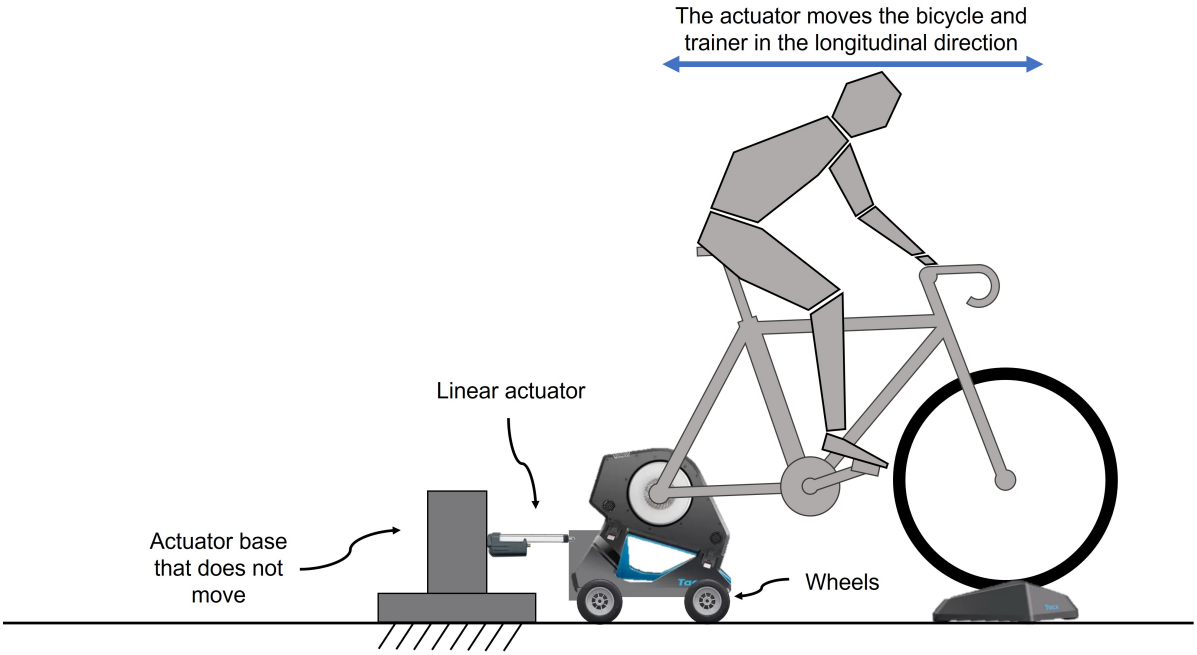

Figure (5.1) A conceptual idea of an actively controlled longitudinal moving indoor trainer setup.

The cyclist, bicycle, and indoor trainer are seen as one rigid body in this concept. However, in the real world, the cyclist is able to apply forces to the bicycle as we saw in the study of Stone and Hull and the motion capture study performed in chapter 3 [20]. Every cyclist behaves differently on the bicycle and therefore, exerts forces on the bicycle in another way. Measuring these forces in a bicycle for the consumer would be very difficult as a user must apply sensors to his or her bicycle. This will most likely be too expensive as well.

When considering the cyclist, bicycle, and trainer as one body internal forces do not have to be accounted for when calculating the actuator force since internal forces do not cause a change in motion of a body's center of mass. However, these forces can counteract or supplement the actuator force resulting in other motions than when only the actuator force is present. The centers of mass of the bicycle plus trainer and that of the cyclist can move relative to each other, as discussed in section 4.2. This relative motion is assumed to apply a counterforce to the actuator resulting in the notch shown in Figure 3.6.

For the concept of Figure 5.1, a free-body diagram is made as well, which is illustrated in Figure 5.2.

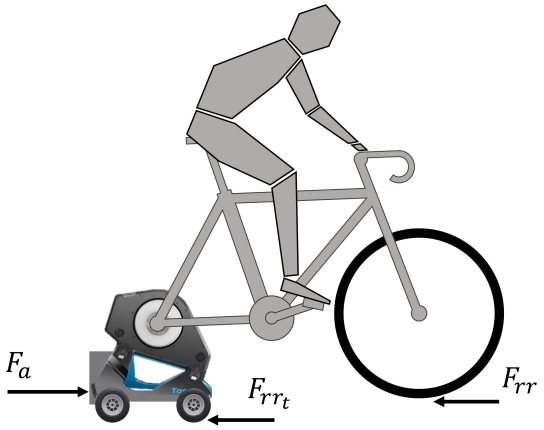

Figure (5.2) A free-body diagram of the concept active-controlled longitudinal motion trainer setup

Where F_a is the force that the linear actuator applies, F_{rr_t} is the rolling resistance of the rolling trainer, and F_{rr} is the rolling resistance of the front wheel. If the motion of the indoor setup is realistic it must hold that:

$$\ddot{x}_{indoor} = \ddot{x}_{outdoor} \tag{5.1}$$

We know that the acceleration of an outdoor bicycle is:

$$\ddot{x}_{outdoor} = \frac{F_p - (F_d + F_g + F_{rr_o})}{m_c + m_b} \tag{5.2}$$

And that the acceleration for the concept setup is:

$$\ddot{x}_{indoor} = \frac{F_{actuator} - (F_{rr_t} - F_{rr_i})}{m_c + m_b + m_t} \tag{5.3}$$

Where m_t is the mass of the indoor trainer. If we then write out Equation 5.1 it leaves us with:

$$\frac{F_p - (F_d + F_g + F_{rr_o})}{m_c + m_b} = \frac{F_{actuator} - (F_{rr_t} + F_{rr_i})}{m_c + m_b + m_t} \tag{5.4}$$

Isolating the actuator force term F_a gives:

$$F_a = \frac{(m_c + m_b + m_t)(F_p - (F_d + F_g + F_{rr_v}))}{m_c + m_b} + F_{rr_i} + F_{rr_t} \tag{5.5}$$

The "Magic Equation" to translate outdoor cycling forces through a linear actuator to indoor cycling is now given as Equation 5.5. m_c, m_b, m_t are the masses of the cyclist, bicycle, and trainer and are set parameters but can vary for every cyclist.

F_p is the virtual propulsion force. This force can be calculated by dividing the torque measured by the trainer by the radius of the rear wheel. Because the torque is measured by the trainer around the rotation axis of the flywheel, the gear ratio does not have to be accounted for.

F_d is the virtual aerodynamic drag force that is based on the virtual cycling velocity. If we assume the initial virtual velocity is equal to 0 then F_d initial is 0 as well. For the time stamp after $t = 0$ the virtual acceleration can be calculated with the virtual rolling resistance, virtual gravitational resistance, and virtual propulsion force:

$$\ddot{x} = \frac{F_p - (F_{rr_v} + F_g)}{m_c + m_b} \tag{5.6}$$

Integrating the virtual acceleration leaves us with the virtual velocity which is used to calculate the aerodynamic drag for the next time stamp. Therefore, the virtual aerodynamic drag force is based on the virtual velocity of the previous time stamp.

F_g and F_{rr_v} are the virtual gravitational and rolling resistance forces, which depend on the mass of the cyclist and bicycle as well as on the virtual slope angle. The masses are known and the slope angle depends on the course that is ridden, meaning that the trainer will communicate what the slope angle is per time stamp. Therefore, the rolling and gravitational resistance are also calculated per time stamp.

To simplify the equation we combine the virtual forces to one sum of virtual forces, F_{vir}:

$$F_a = \frac{(m_c + m_b + m_t) \cdot F_{vir}}{m_c + m_b} + (F_{rr_i} + F_{rr_t}) \cdot sgn(\dot{x_t}) \tag{5.7}$$

Because the trainer is on wheels and the front wheel of the bicycle rolls over the floor two real-world rolling resistance forces are present in the ”Magic Equation”, F_{rr_i} the rolling resistance of the front wheel and F_{rr_t} the rolling resistance of the trainer. The rolling resistance of the front wheel is assumed to have a C_{rr} of 0.004 and is set as a constant value based on the mass of the cyclist, bicycle, and trainer. Whereas, the C_{rr} of the trainer must be determined (Appendix B). The direction of the real-world rolling resistance forces depends on the sign of the velocity of the trainer setup. Hence the $sgn(\dot{x_t})$ term in Equation 5.7

Since this thesis concerns longitudinal motion in indoor trainers, that naturally are used indoors, we need to keep in mind that the space for motion is restricted. Therefore, a requirement for a longitudinally moving trainer setup is the allowed motion is $\pm$ 20 cm. A feature in the simulator controller must be implemented to avoid the trainer setup exceeding $\pm$ 20 cm displacement.

The space restriction does not allow large motions that are present in outdoor cycling. Therefore small longitudinal motion is the most important performance metric for the simulator controller. This small motion is the intr-pedal stroke range of motion as was described in section 3.2.

There are no requirements compiled for the actuator force since this thesis also aims to discover what actuator force is necessary to actuate the trainer setup in the desired way. The specifications of the actuator will be established in a follow-up study of this thesis.

Now the equation on how to translate real-world forces to indoor cycling through an actuator is defined, the ”Magic Equation”, a controller to generate the variables and simulate the trainer setup motion can be designed. The simulator controller will be discussed in chapter 6.

6

Simulator controller

The simulator controller that controls the longitudinal motion of an indoor trainer will be discussed in this chapter (chapter 4). Since the longitudinal moving trainer setup will not be built during this thesis, the controller will simulate the motion of the bicycle, cyclist, and trainer as one system.

The controller is designed in Simulink (Mathworks, Natick, Massachusetts, USA). Simulink is a programming environment for graphically designing models and simulations for multi-domain dynamical systems. The Simulink block diagram is discussed extensively in Appendix A. This chapter will address a more generic block diagram to describe the simulator controller's flow. The block diagram is shown in Figure 6.1.

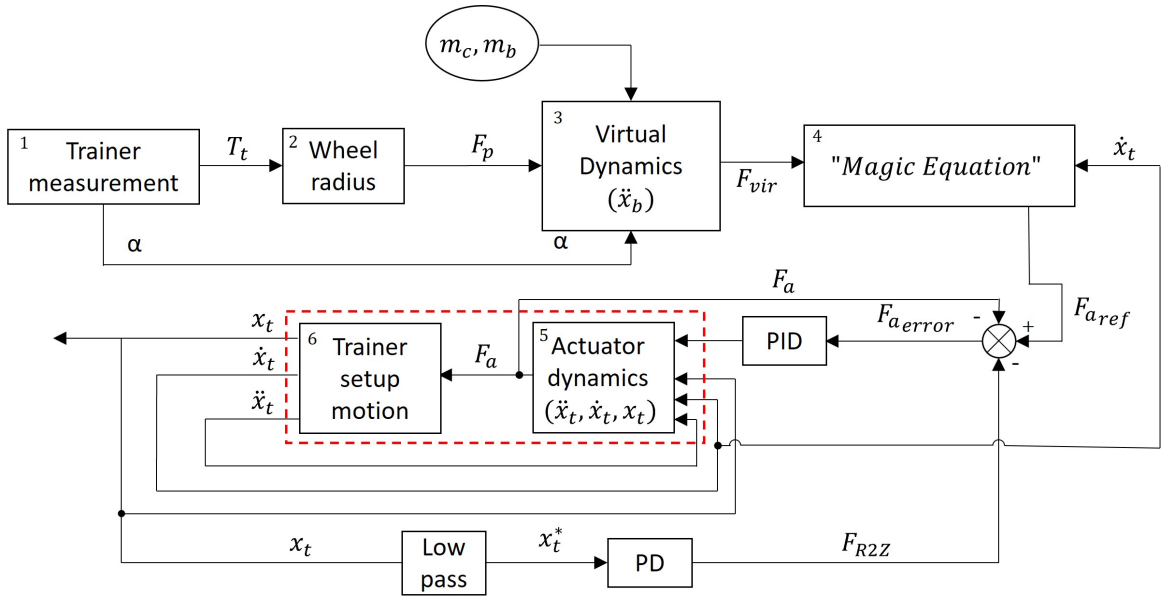

Figure (6.1) Block diagram of the longitudinal trainer motion simulator controller. The input variables are 1) Torque T_t measured by the smart indoor trainer around the axis of the flywheel which varies per timestamp (block 1). 2) The virtual slope angle $alpha$ communicated by the trainer every time stamp (block 1). 3) The mass of the cyclist, bicycle, and trainer which are set to a constant based on the cyclist. The simulator controller calculates the virtual sum of forces F_vir in block 3 and feeds that to the "Magic Equation" to determine the reference actuator force $F_{a_{ref}}$ (block 4). $F_{a_{ref}}$ is the reference signal for the actuator dynamics in block 5, where the mechanical and electromechanical losses are accounted for to determine the actual actuator force F_a. That actuator force actuates the trainer setup through block 6 which is an algebraic equation. The red outlined blocks resemble the plant in the simulator controller.

The input signals for the controller are torque which is measured by the smart indoor cycling trainer and virtual slope angle which is also determined by the trainer (block 1). The first step of the controller is to determine the virtual propulsion force. This is done by dividing the torque (T_t) by the radius of a bicycle wheel (block 2), which is 0.35m.

Now the propulsion force (F_p) is known the virtual dynamics of the bicycle can be calculated in block 3. The output of this block is the sum of the virtual forces as described in Equation 5.7. The sum of these forces contains the virtual propulsion force, virtual aerodynamic drag force, virtual rolling resistance force, and virtual gravitational force. The propulsion force is already calculated in the previous part of the controller, so only the virtual resistance forces are to be calculated so Equation 5.7 can be completed for block 4, the ”Magic Equation”.
Both the rolling and gravitational resistance depend on the mass of the cyclist and bicycle, as well as the slope angle. Therefore, these forces do not depend on the state of the virtual cyclist. However, the aerodynamic resistance does depend on this virtual state, since the aerodynamic drag resistance is a function of the velocity.
The controller assumes an initial velocity of 0 m/s, therefore the F_d is equal to 0 N for t_0. However, the propulsion, rolling resistance, and gravitational resistance forces are not equal to 0 and can therefore lead to a virtual acceleration. The virtual acceleration is calculated in block 3 as is defined in Equation 6.1:

$$\ddot{x}_b = \frac{F_p + F_d + F_{rr} + F_g}{m_c + m_b} \tag{6.1}$$

Since we know the virtual acceleration ($\ddot{x}_b$), we can integrate this value over the time step. This integration results in the virtual velocity $\dot{x}_b$, assuming that the initial velocity is 0. Since the virtual velocity for t_1 is known the virtual aerodynamic drag value can be calculated for t_1 since this is a function of $\dot{x}_b$. Block 3 is, therefore, a second-order ordinary differential equation.

When a cyclist cycles outdoors aerodynamic drag and gravitational resistance act both on the cyclist and the bicycle, meaning that the bicycle and cyclist are both ’pushed back’ by those resistances. In this thesis concept, the actuator substitutes the aerodynamic drag and gravitational resistance force through an actuator that only works on the bicycle. To avoid that the actuator pulls the bicycle with the combined force that an outdoor cyclist will experience, the aerodynamic drag and gravitational resistance forces are downscaled to the contribution that the bicycle properties would have in the real-world to these forces. This is done to avoid that the actuator will apply unrealistically amounts of force to the bicycle, which might lead to the feeling that the bicycle is pulled or pushed from underneath the cyclist.

The gravitational resistance is downscaled to the percentage of the bicycle’s weight with respect to the mass of the cyclist and bicycle. Whereas the aerodynamic drag is downscaled to 28% of its total value since this is the contribution of a bicycle to aerodynamic drag found in literature [37].

Block 4 contains the ”Magic Equation” that translates the virtual forces F_vir to the actuator reference force $F_{a_{ref}}$ as we defined in Equation 5.7.

The working direction of the rolling resistance of the trainer F_{rr_t} is the opposite of the velocity direction of the trainer setup. This means that the block where Frr_t is calculated depends on the state of the trainer setup. Therefore, $\dot{x}_t$, the trainer setup velocity, is the input signal for the block.

The equation to calculate F_{rr_t} is:

$$F_{rr_t} = C_{rr_t} \cdot 9.81 \cdot (m_c + m_b + m_t) \tag{6.2}$$

Where C_{rr_t} is the rolling resistance coefficient of the trainer setup and is determined to be 0.033 (Appendix A).

The rolling resistance for the front wheel of the bicycle is calculated in the same way but then for a C_rr of 0.004, which is used to calculate the virtual rolling resistance as well.

Completing the ”Magic Equation” results in the actuator reference force $F_{a_{ref}}$ which will be fed to block 5 to determine the actuator dynamics.

The average value of F_{a_ref} is not equal to 0 as displayed in Figure 6.2. This means that the average acceleration of the simulated trainer setup will also be unequal to zero. Therefore, large displacements over time can occur in the simulations. To avoid this the actuator reference force must be detrended so that the average value is equal to zero. This detrending is done using the Matlab function *sgolayfilt*, which is a Savitzky-Golay filter. The order was set to 1 and the frame length to times the sampling frequency plus 1 ($2Fs + 1$. The frame length must be an odd number, hence, the summation with 1.

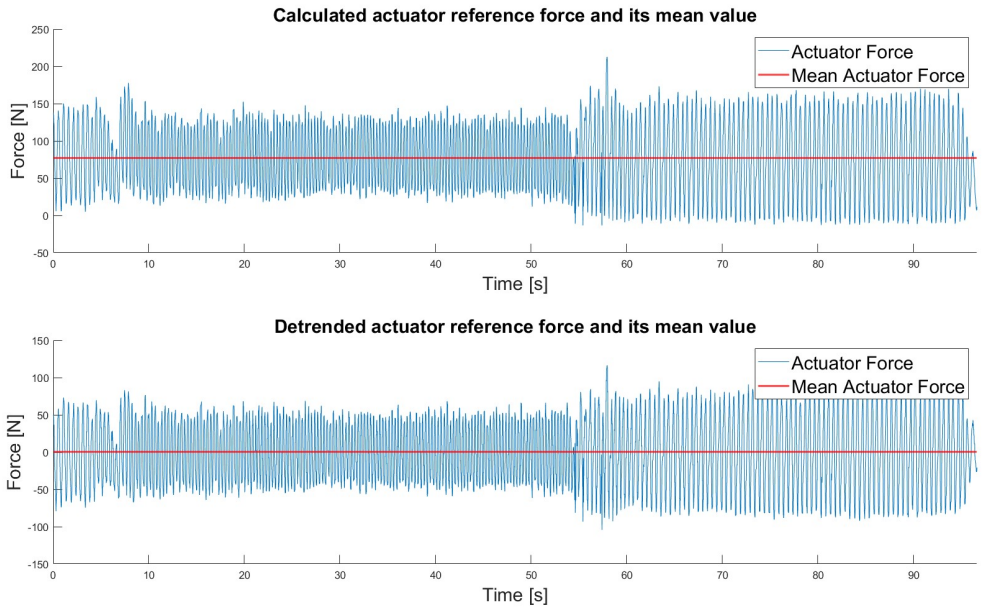

Figure (6.2) The calculated actuator reference force and its average value in the upper plot. The lower plot displays the detrended actuator reference force and its average value. The detrending was done with the Matlab function *sgolayfilt($F_{a_{ref}}$,1,$(2 \cdot Fs) + 1$)*

Figure 6.2 shows that by detrending the reference actuator forces the average value becomes 0. Therefore, there will be no displacement of the simulated indoor trainer setup over time.

Before the signal is fed to the actuator dynamics block, it passes a PID controller to account for the error between de reference signal $F_{a_{ref}}$ and the output force F_a of the actuator dynamics block. The output of the PID controller block is defined as u. The proportional gain was set as 0.5, the integral gain as 50, and the Derivative as 0. The tuning of the PID controller was done through trial and error whilst observing which setting resulted in the least amount of error between $F_{a_{ref}}$ and F_a.

The block does not resemble a real actuator which would have current and voltage as an input signal. Instead, there was chosen to mimic the dynamics of an actuator as closely as possible by implementing damping, stiffness, actuator mass, and electromechanical delay. In this way, we try to calculate the mechanical losses of the actuator as well as possible, to determine the way in which the trainer setup would actually be actuated by the actuator. The output force of the actuator is described in the following equation:

$$F_a = u + m_a \cdot \ddot{x}_t + \frac{1}{c} \cdot \dot{x}_t + k \cdot x_t \tag{6.3}$$

Where m_a is the mass of the actuator piston, c is the damping coefficient and k is the stiffness of actuator piston. The force that needs to be overcome as a result of actuator stiffness is not the same as that of a spring force, which is $c \cdot \dot{x}_t$. If that were the case it would mean that a higher actuator stiffness would lead to more spring force. Whereas, a stiffer actuator would mean that there are fewer mechanical losses. Therefore, the term that accounts for actuator stiffness is $\frac{1}{c} \cdot \dot{x}_t$.
A real actuator needs some reaction time due to electromechanical delays in the control system. Therefore, a delay is built into the actuator dynamics block, which is 10ms.

Note that the actuator dynamics depend on the state of the trainer setup, hence the subscript t. This is because the actuator piston is rigidly connected to the indoor trainer and the controller assumes there are no mechanical losses in that connection.

Since the actuator is rigidly connected to the trainer it has the same displacement as the trainer setup, and consequently the same velocity and acceleration, hence the use of x_t, $\dot{x}_t$, and $\ddot{x}_t$

The output force of the actuator dynamics block F_a is then fed to the trainer setup dynamics block to calculate the state of the trainer setup. The acceleration of the trainer setup, $\ddot{x}_t$, is determined by dividing F_a by the mass of the cyclist, bicycle, and trainer. By integrating $\ddot{x}_t$ the velocity, $\dot{x}_t$ is determined. A second integrator results in x_t, the position of the trainer setup. Figure 6.3 displays a schematic illustration that describes the state of the trainer setup.

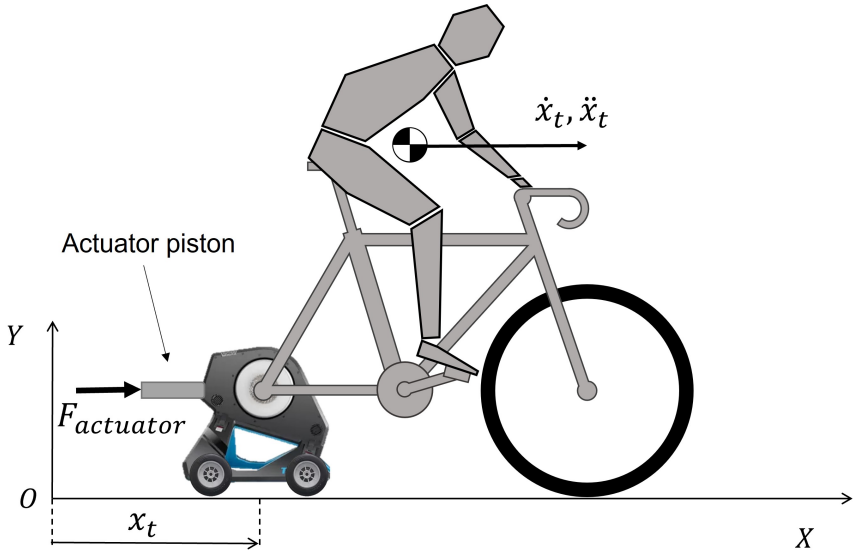

Figure (6.3) State description of the trainer setup, where x_t is the position of the trainer, $\dot{x}_t$ is the velocity of the trainer, and $\ddot{x}_t$ is the acceleration of the trainer.

Over time the trainer setup can drift away from its setpoint, with the risk the trainer setup will reach the end-stops of the actuator. To avoid this a return-to-zero model is implemented in the block diagram. This model consists of a first-order low-pass Butterworth filter with a cutoff frequency of 0.1 Hz and a PD controller in which the proportional and Derivative gain were both set to 100. The tuning of the filter and controller was done by trial and error whilst observing which settings are optimal to mitigate the drift of the trainer setup.

The low-pass filter identifies the drift of the trainer setup without the intra-pedal stroke motion. Figure 6.4 displays the position of the trainer setup and its drift over time.

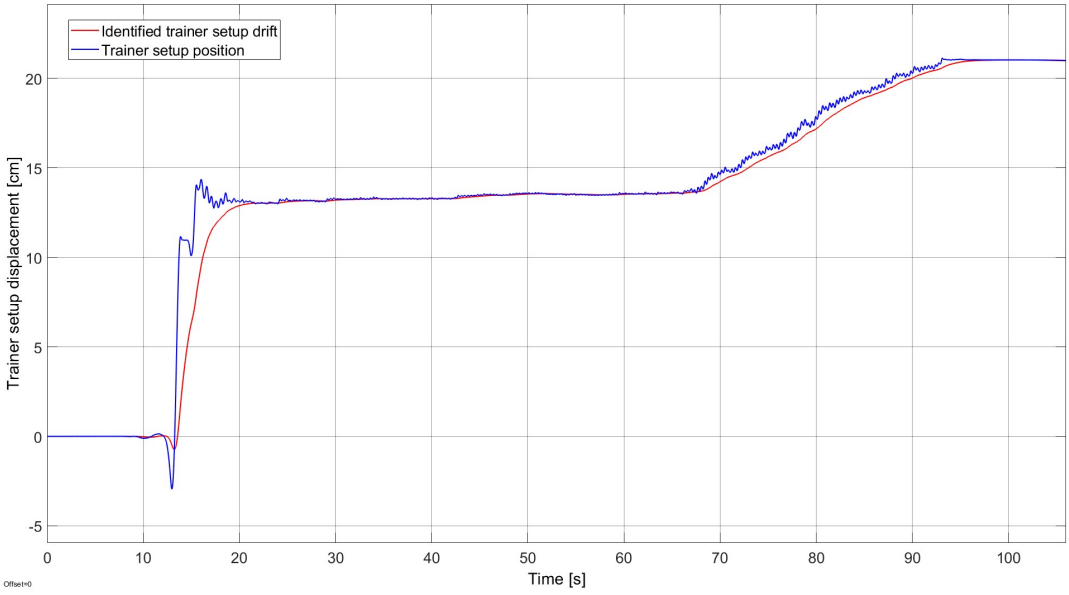

Figure (6.4) The simulated position of the trainer setup without compensation for drift. The blue line is the position and the red line is the low-pass filtered trainer setup position to identify the drift.

The drift $\dot{x}_t^*$ is then ran through a discrete PD controller Figure 6.5. The PD controller determines how fast the controller compensated for drift. If the drift is small and/or slow little compensation is needed. However, if the drift is large and/or fast the controller needs to compensate quicker and more. For that purpose, a PD controller is used.

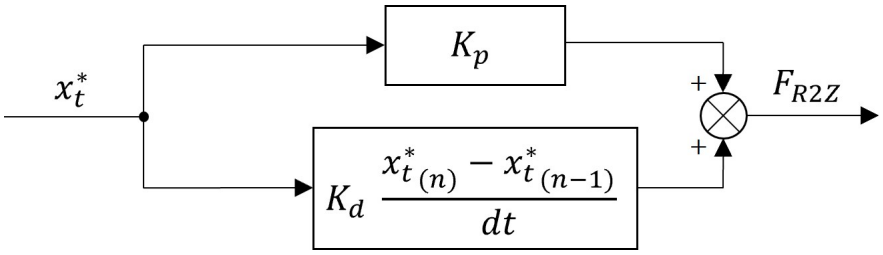

Figure (6.5) The discrete PD controller that eliminates the drift of the trainer setup.

The proportional part ensures that the magnitude of the drift is multiplied with a certain Nm^{-1} gain (K_p). The derivative part of the PD controller applies a Nm^{-1} gain (K_d) to the derivative of the drift. If the trainer setup drifts fast then the value of the derivative part is large. In that way, the PD controller has a stronger response to fast drift changes in trainer setup drift.

The sum of the P and D part of the PD controller is the force, F_{R2Z} that is required to return the trainer setup to its setpoint without affecting the intra-pedal stroke motion. The result of the return-to-zero model is shown in Figure 6.6. The same data was used as for Figure 6.4.

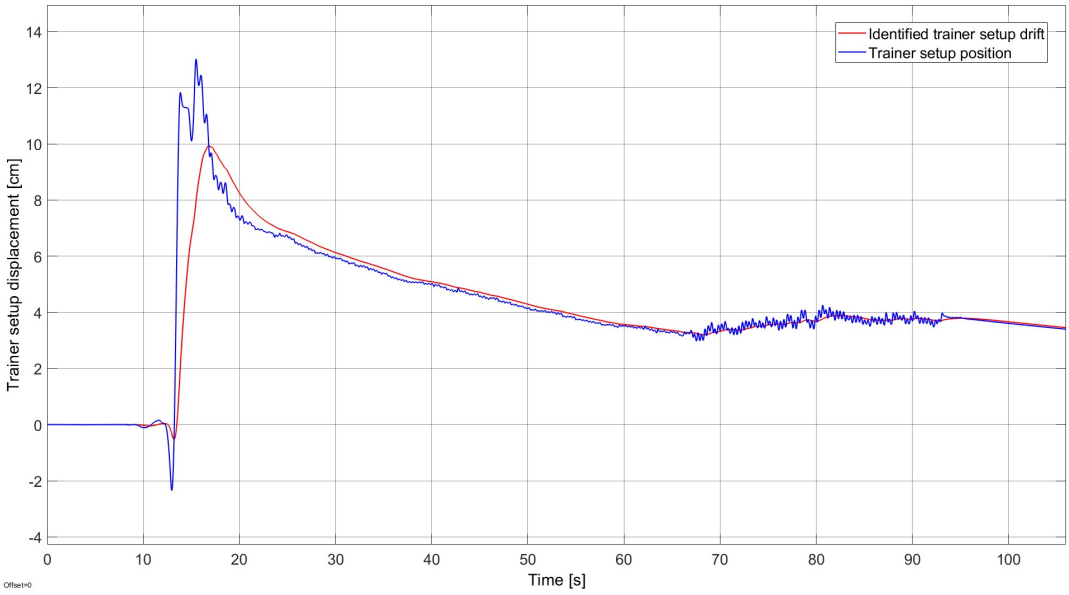

Figure (6.6) Drift compensated trainer setup position through the return-to-zero model.

Note that the drift of the identified drift, the red line in Figure 6.6, does not overlap the position curve of the trainer setup exactly. This is because the low-pass filter has a delay compared to its input signal. For that reason, the trainer setup has some time to move before the return-to-zero model starts pushing it back to its setpoint. Hence, the peak in simulated trainer setup displacement at around 15 seconds in Figure 6.6

Now the simulator controller has been designed data must be acquired to run the simulator controller and assess its performance in translating outdoor longitudinal cycling dynamics to an indoor cycling setup. This is done in the following chapter 7.

7

Data collection method

7.1. Methods

To assess the longitudinal cycling motion simulator controller performance, input data must be collected. The input signal for the simulator controller will be torque around the flywheel of the indoor smart turbo trainer. This input is chosen because it is measured by the trainer itself, so no other accessories have to be added to measure force or torque elsewhere on the bicycle. It also eliminates the need to know the gear ratio that is ridden, because the torque only needs to be divided by the radius of a rear cycling wheel to calculate virtual propulsion force.

Since the input data is torque around the trainer's flywheel, it is most convenient to collect that data on a trainer as well. The trainer that was used is the Tacx Neo 2T Figure 7.1. This is a high-end smart cycling indoor trainer and is, therefore, able to produce a large resistance variety to simulate different cycling scenarios such as steep climbs (25% slope).

For the torque data collection 4 different test subjects were measured during different cycling situations on the static smart turbo trainer:

1. 0% slope seated and standing cycling
2. 2.5% slope seated and standing cycling
3. 5% slope seated and standing cycling
4. 10% slope seated and standing cycling
5. 15% slope seated and standing cycling
6. 20% slope seated and standing cycling
7. 25% slope seated and standing cycling

7.1.1. Participants

The 4 participants measured included 1 female and 3 males with an average weight of 73.13 kg and an average age of 31.5 years. The test subjects were trained to well-trained cyclists. Table 7.1 Gives an overview of test subject characteristics for the 4 test subjects that have participated in the data collection experiments.

Table (7.1) The characteristics of the test subjects that participated in the data collection experiments.

Test subject	Gender	Weight in kg	Age in years	Cycling level
1	M	91	27	Well trained
2	F	59	43	Trained
3	M	71.5	25	Trained
4	M	71	30	Well trained

7.1.2. Equipment

The data was collected through a standard indoor training setup (Figure 7.1) using the following equipment:

1. A road bicycle with 50/34 chainrings and 11 to 34 sprocket cassette.
2. A Tacx Neo 2T indoor trainer (Tacx by Garmin, Oegstgeest, Netherlands)
3. Rasp Tacx device data collection software (Tacx by Garmin, Oegstsgeest, Netherlands).
4. A Custom antenna to connect with the trainer (Tacx by Garmin, Oegstsgeest, Netherlands).
5. A laptop

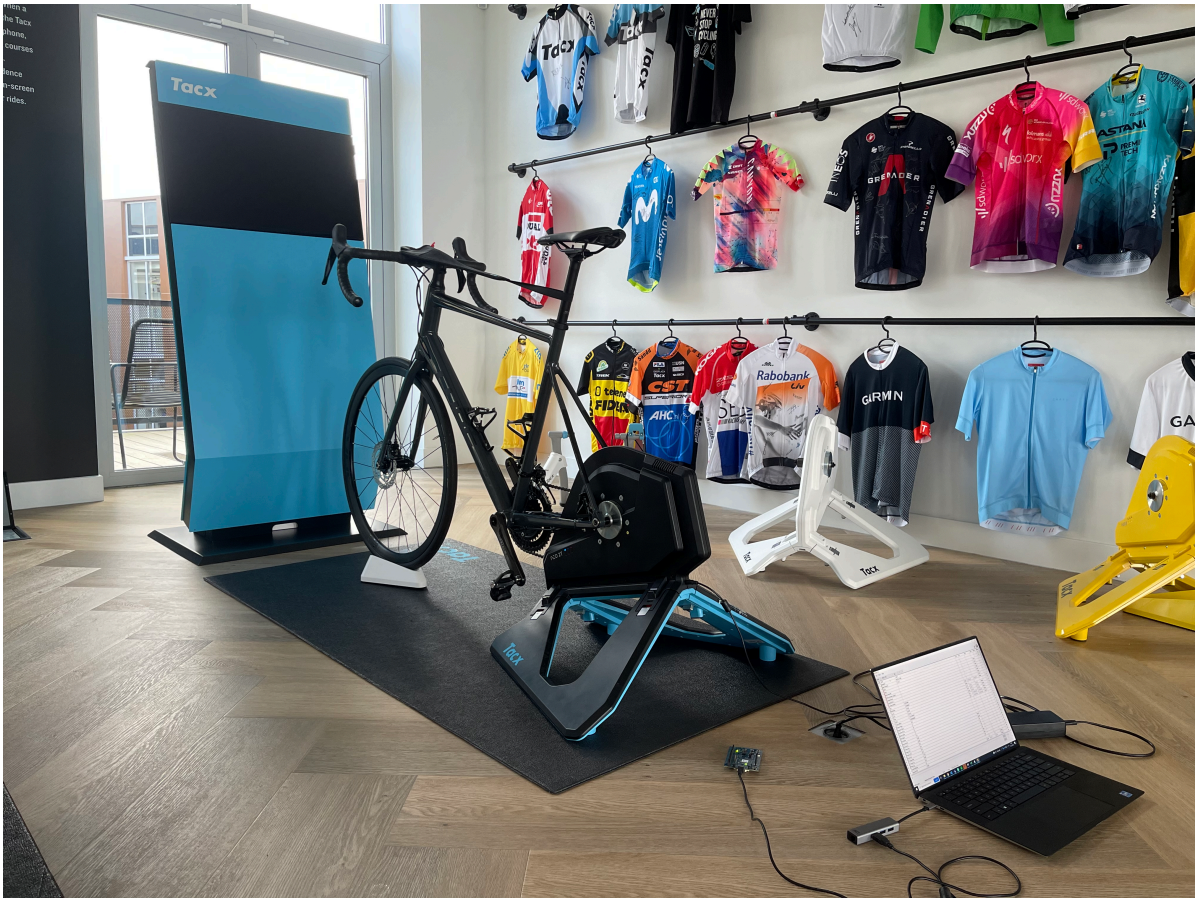

Figure (7.1) The Tacx Neo 2T setup to collect torque data through a wireless Rasp connection.

A common modern road bicycle was used to mount to the Tacx Neo 2T. For every test subject, the correct frame-size bicycle was installed with a proper gear ratio for every slope angle to ensure the most realistic cycling as possible. The Tacx Neo 2T is a high-end smart indoor trainer that is capable of generating a resistance torque around the flywheel axis of 89 Nm. The data is sent by making wireless contact with the trainer through an in-house Tacx communication application called Rasp Figure 7.2. The Tacx Neo 2T was controlled through Rasp and the torque measured by the trainer was also collected with the use of Rasp. The sampling frequency of the data collection was 64 Hz. Rasp does also log the slope percentage. In Rasp, the mass of the test subject and the bicycle were set so that the trainer can calculate the corresponding resistance forces for the different data collection blocks. The mass of the bicycle was set to 7.5 kg for all test subjects. The C_dA value was set at 0.51 m^2 and the C_{rr} value was set to 0.004 as this are the standard values Tacx uses.

Figure (7.2) The wireless connection with the Tacx Neo 2T and Rasp through a Tacx custom-made antenna.

7.1.3. Protocol

The data collection protocol consists of riding 7 virtual slope angles from 0% to 25% on the Tacx Neo 2T in a random order to minimize fatigue influence. During every incline, the cyclist tried to find a suited gear for the cycling situation and tried to maintain a steady-state whilst seated cycling for 30 seconds. Thereafter, the test subject did the same but then for 30 seconds of steady-state standing cycling. The stepwise measurement protocol is as follows:

1. The Tacx Neo 2T was connected to Rasp in which the weight of the test subject and slope angle was set.
2. The test subject took place on the bicycle and the data logging was turned on in Rasp.
3. The test subject selected a suitable gear ratio and found a steady-state cycling pace whilst remaining in the saddle.
4. After the seated cycling block, the test subject was asked to adopt a standing cycling position and find a steady-state pace for another 30 seconds.
5. After the standing cycling block the slope angle was set to 0% so that the test subject could recover from the measurement.
6. When the test subject indicated that he/she was ready for the next slope measurement the slope was set to the next value and the previous steps were repeated until the 7 slopes were measured.
7. The collected data was then saved automatically by Rasp in a *.txt* file, including the time stamp, trainer-measured torque, cadence, and mass of the cyclist.

The data collection time was short because the blocks at the high slope percentages are very demanding for the test subjects. It may be possible that a test subject could not finish the test protocol if the blocks were longer or that the fatigue had too much of an impact on the final blocks of the measurement protocol. To avoid fatigue affecting the high slope cycling performance too much, the order of the incline angle on which the test subject rode was randomized per participant.

With all the data collected for the 4 test subjects, it was run through the simulator controller to assess its performance in translating longitudinal outdoor cycling forces to an indoor cycling setup. The results of the simulation are given in chapter 8.

8

Results

As the simulator controller needs torque data as the input signal to run, this data was acquired with the tests described in chapter 7. Before heading to the simulation results the input torque data will be shown in Figure 8.1 & Figure 8.2. Figure 8.1 displays the input torque and the cadence for a simulation of riding a 0% virtual slope. Whereas, Figure 8.2 displays those values for a 25% slope. The figures clearly explain that if the slope increases and, therefore, the resistance the torque increases and the cadence decreases.

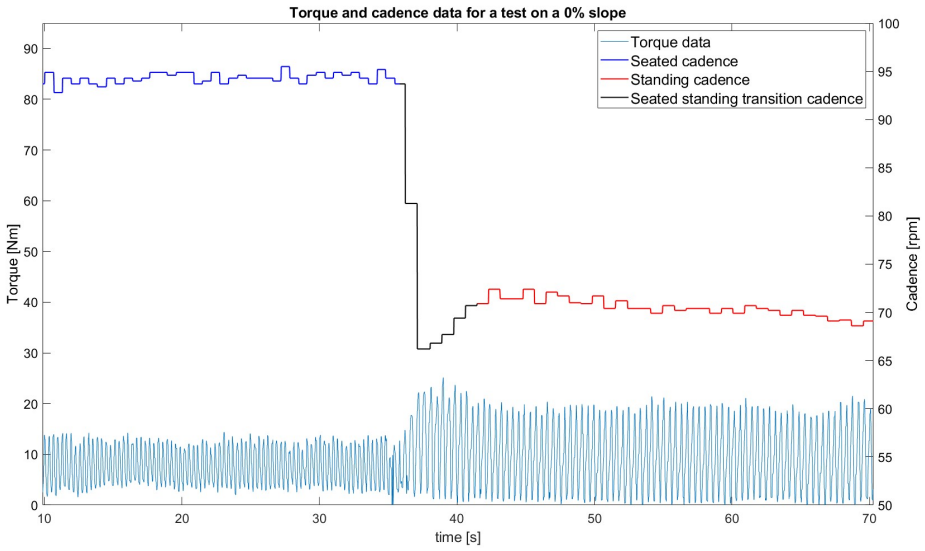

Figure (8.1) The torque input data for the simulator controller and the corresponding cadence for a slope of 0%. The color of the cadence curve indicates if the cyclist is in a seated or standing position or if she/he is in the transition phase between seated and standing cycling.

Figure 8.1 shows the two parts of the measurement, the seated and the standing cycling block. In between the blocks, there is a transition phase in which the test subjects change from a seated to a standing cycling position and settle at a steady-state again.

The cadence during the measurement is also given. Note that the color of the curve changes to indicate if the cyclist is in the saddle (blue), transfers to steady-state standing (black), and standing cycling (red).

For cycling on a 0% virtual incline in a seated cycling position, the average torque value was 7.83 Nm whereas the standing cycling torque was 9.48 Nm for average cadences of 93.93 and 70.45 rpm, respectively.

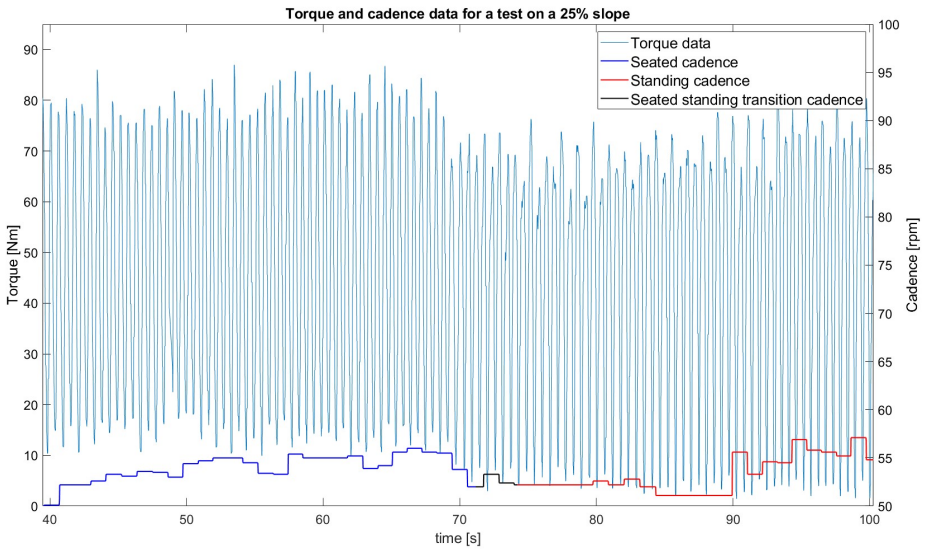

Figure (8.2) The torque input data for the simulator controller and the corresponding cadence for a slope of 25%. The color of the cadence curve indicates if the cyclist is in a seated or standing position or if she/he is in the transition phase between seated and standing cycling.

Figure 8.2 shows the torque input signal for a 25% virtual slope simulation. It clearly stands out that the torque is much higher for riding a 25% incline compared to a 0% incline. The average torque for the seated block was 44.90 Nm with an average cadence of 53.86 rpm. Whereas for the standing block, the average torque was 44.51 Nm with an average cadence of 53.46.

In this chapter the results of the simulations will be given. The simulation results consist of 7 data sets per test subject with different slope angles. Within each slope angle dataset, a seated and standing cycling block are included in which steady-state cycling was reached with a fixed gear ratio.

An overview of test person 1 performance during the data collection experiments is given in Table 8.1. For increasing slope angle the peak torque and average power during the seated and standing blocks. Whereas, the cadence decreased as the incline increased. However, for the steepest virtual slope angle of 25%, the peak torque values and avg power were lower than those of the 20% and 15% inclines.

Table (8.1) Am overview of test subject 1 for all ridden virtual slope angles of the measured torque peaks for seated and standing cycling, the seated and standing cadence rpm, and the average power per block of seated and standing cycling.

Slope	Seated peak torque	Standing peak torque	Steated cadence	Standing cadence	Seated avg. Power	Standing avg. Power
0%	18.99	26.66	92.42	87.13	100.07	94.12
2.5%	26.61	35.14	88.23	82.29	137.71	118.80
5%	36.97	49.62	76.23	67.25	172.66	145.62
10%	58.18	69.97	71.83	59.04	267.25	214.35
15%	83.49	88.51	66.67	58.49	354.50	305.52
20%	90.37	87.56	64.46	55.45	373.85	284.79
25%	88.29	84.85	61.38	54.70	348.51	274.70

Figure 8.3 displays the virtual velocity and the virtual resistance per ridden virtual slope angle for every test subject. The solid lines resemble the seated cycling blocks of the measurement whereas the dashed lines are the standing cycling blocks. The velocity decreases as the resistance increases, which is the case for all test subjects. The difference between the standing and seated virtual velocity during the simulations is only slight. However, it is important to display it since large differences in virtual velocity might affect the simulation results.

The resistance force varies as the virtual velocity varies since the aerodynamic drag force depends on velocity, meaning that if the virtual velocity decreases, the total resistance will decrease accordingly. Only small virtual velocity changes are observed between seated and standing cycling, leading to small changes in resistance as well.

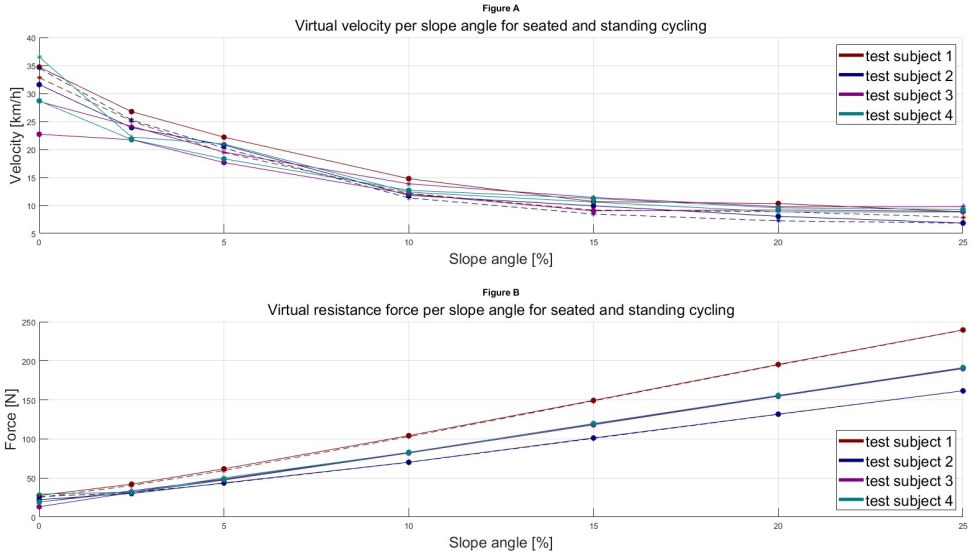

Figure (8.3) **Figure A** displays the mean virtual velocity per ridden virtual slope angle, where the solid lines resemble the seated cycling blocks and the dashed lines are the standing cycling blocks of the measurement. **Figure B** displays the virtual resistance force per virtual slope angle, where the solid lines resemble the seated cycling blocks and the dashed lines are the standing cycling blocks of the measurement.

The peak torque values of all the test subjects are given in Figure 8.4. For the seated blocks, the peak torque values increase as the slope angle increases for every test subject but test subject 1. For the standing blocks only test subject 3 has increasing peak torque over all the incline percentages. By giving an overview of the torque data for every test subject for every slope for both seated and standing cycling we can use this as one of the reference figures to determine if the simulations were performed correctly. If the torque is low and the motion of the simulated trainer setup it indicates that the simulation is not valid since we expect low motion with low torque cycling.

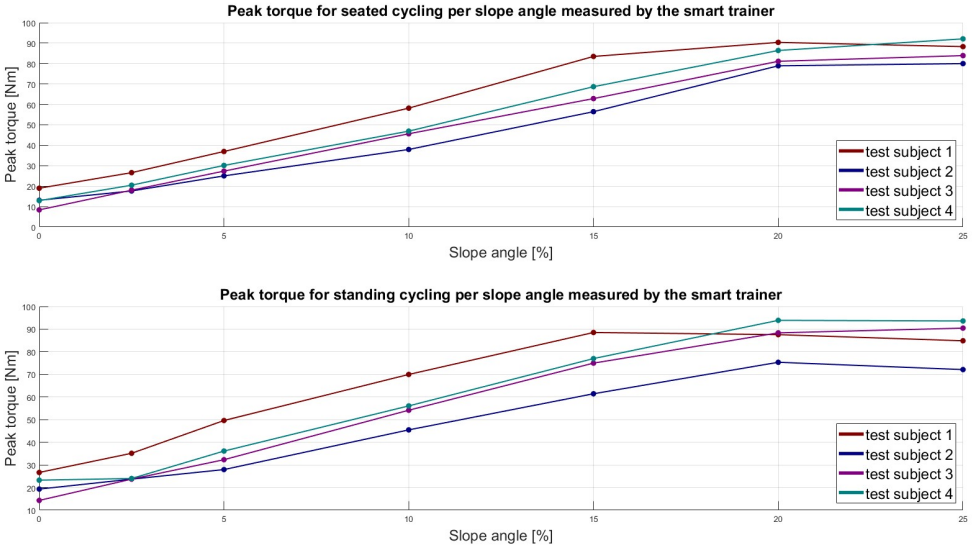

Figure (8.4) The Peak torque values of all test subjects for different virtual inclines. The upper plot displays the seated block of the measurement whereas, the bottom plot displays the standing cycling peak torque values.

The gathered torque data was fed to the simulator controller that is described in chapter 4. The output of the controller is trainer setup displacement x_t and this output is given in Figure 8.5 for test subject 2, who rode a 0% slope. The displacement of the trainer setup is displayed with the input signal, torque, in the same figure.

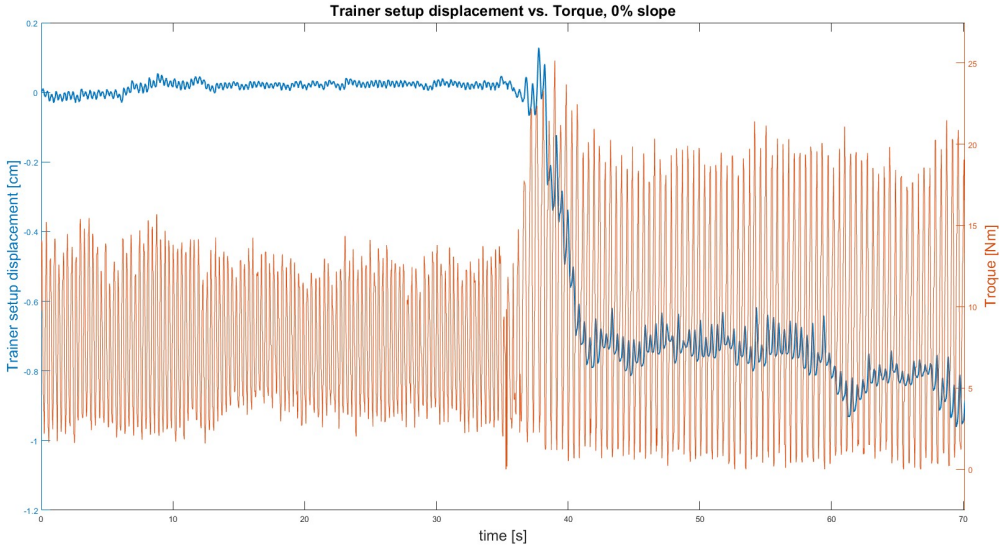

Figure (8.5) The simulation result of test subject 2, riding a 0% incline

The first part of the data is seated, at 35 seconds a transfer is made to the standing position, hence the jump in the displacement at that point. The torque decreases for a moment when transferring to a standing position which causes the bicycle to decrease and, therefore, the trainer setup has a displacement in the negative direction.

The cadence decreases but the torque increases, as can be seen in the torque curve. The trainer setup range of motion during one pedal stroke also increases for the standing part of the simulation. The minimal position with respect to the setpoint 0, is -0.86cm and the maximal position is 0.135cm for the trainer setup.

The trainer setup motion is caused by the actuator which applied a maximum force of 60.80N and a minimal force of -60.82N. The applied force results in a maximal acceleration of 0.69 m/s^2 of the simulated trainer setup. Whereas, the maximal deceleration of the trainer setup is simulated to be 0.69 m/s^2. The mean displacement of the trainer setup per pedal stroke for the seated block is 0.002 cm. For the standing cycling block this 1.36 cm.

Note that the maximal negative displacement of the trainer setup is only -0.86 cm. Therefore, the return-to-zero model does not react aggressively because the offset is small just as the rate at which the offset magnitude increases.

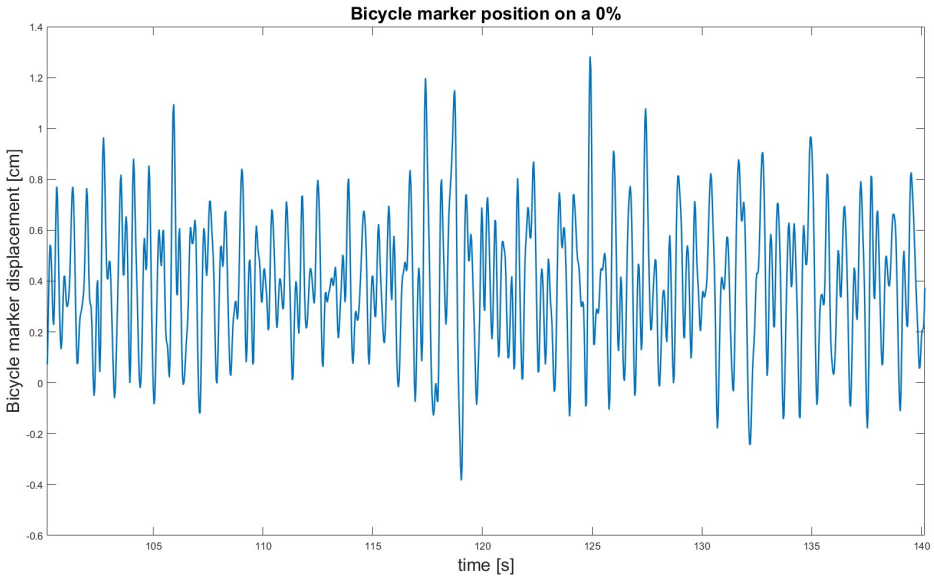

Figure (8.6) The displacement of the bicycle measured on a 0% incline in the motion tracking study performed on a cycling treadmill for test subject 2.

Figure 8.6 shows the marker position of the bicycle whilst cycling on the cycling treadmill with a slope of 0%. We observe that the displacement variance on the treadmill is higher than the simulated displacement in Figure 8.5. However, note that the displacement on the treadmill is that of the bicycle alone and in the simulations, it is the displacement of the bicycle, cyclist, and trainer seen as one rigid body. Figure 8.5 displays the simulation results of the most shallow slope ridden, whereas, Figure 8.7 displays the results of the steepest slope ridden, 25%. Clear differences in the trainer setup displacement can be seen as well as in the torque values.

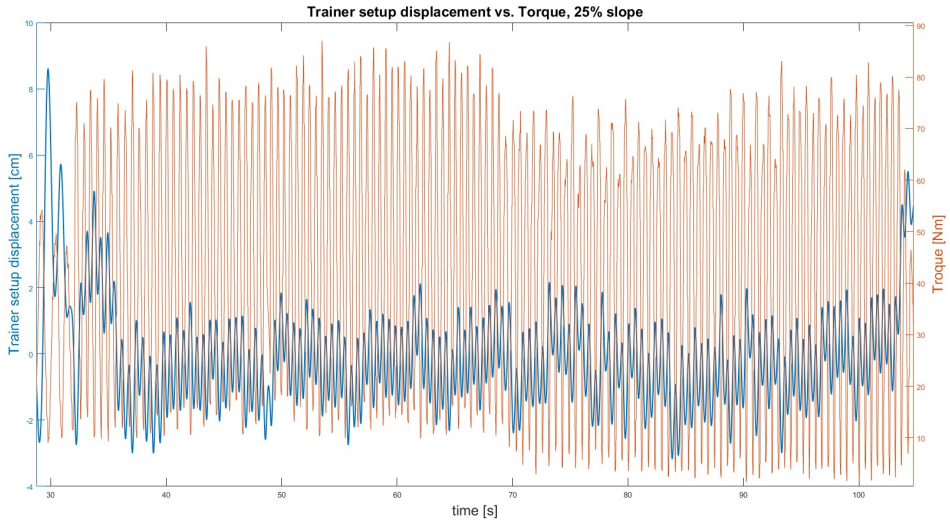

Figure (8.7) The simulation result of test subject 2, riding a 25% incline

The trainer setup motion is caused by the actuator which applied a maximum force of 189.67N and a minimal force of -200.60N. The applied force in a maximal acceleration of 2.16 m/s^2. Whereas, the maximal deceleration of the trainer setup is simulated to be 2.27 m/s^2. The mean displacement of the trainer setup per pedal stroke for the seated block is 0.73 cm. For the standing cycling block, this is 0.71 cm. During the simulation, the maximal displacement with respect to the setpoint of the trainer setup was 8.81 cm and the minimal position was -3.18cm.

Table (8.2) The simulation results of test subject 2 for different slope angles (0% to 25%). F_a is the actuator force in N. $\ddot{x}_t$ is the acceleration of the trainer setup. IPS RoM is the intra-pedal stroke range of motion and is divided into the seated and standing parts of the simulation. x_t is the position of the trainer setup.

Slope	Max F_a	Min F_a	Max $\ddot{x}_t$	Min $\ddot{x}_t$	Intra-pedals troke RoM	Max x_t	Min x_t
0%	57.99	-60.95	0.66	-0.69	0.02 | 0.084	0.04	-1.01
2.5%	62.82	-66.97	0.71	-0.76	0.02 | 0.084	0.86	-2.35
5%	73.39	-86.47	0.83	-0.98	0.144 | 0.554	2	-1.37
10%	116.9	-117.87	1.33	-1.34	0.288 | 1.07	3.2	-1.19
15%	149.42	-165.66	1.7	-1.88	0.754 | 1.701	4.07	-3.2
20%	185.27	-204.88	2.11	-2.33	1.596 | 2.3	6.43	-2.41
25%	189.58	-200.6	2.15	-2.28	2.392 | 2.412	8.18	-3.15

Table 8.2 summarizes the results for all slope angles test subjects rode during the data collection experiments. The higher the slope angle the higher the magnitude of the actuator force F_a became as well. Applies for the acceleration of the trainer setup $\ddot{x}_t$, the intra-pedal stroke range of motion (RoM), and the displacement of the trainer setup x_t.

Figure 8.8 gives an overview of the intra-pedal stroke range of motion for each test subject. The vertical axis displays the displacement per pedal stroke of the simulated trainer setup by the actuator. The displacement is given in cm. The horizontal axis resembles the angle of the vertical incline that was ridden during the data collection experiments.

It can be observed in Figure 8.8 that the intra-pedal stroke trainer setup range of motion plateaus for test subjects 1, 3, and 4. Whereas that of test subject 2 keeps increasing as the slope angle does. The plateauing starts at a 15% slope angle for test subject 1 and at 20 % for test subjects 3 and 4.

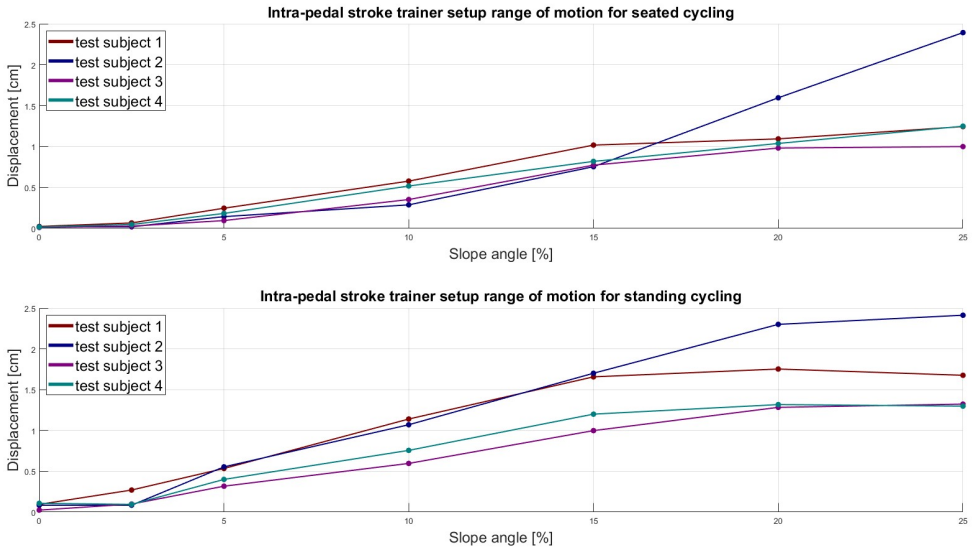

Figure (8.8) An overview of the intra-pedal cycling longitudinal range of motion of the simulated trainer setup for all the test subjects. The upper plot gives the range of motion for seated cycling per measured virtual slope angle. The bottom plot gives the range of motion for standing climbing for all measured virtual slope angles for all test subjects.

Figure 8.9 displays the most important results of the data collection experiments and the trainer setup motion simulation.

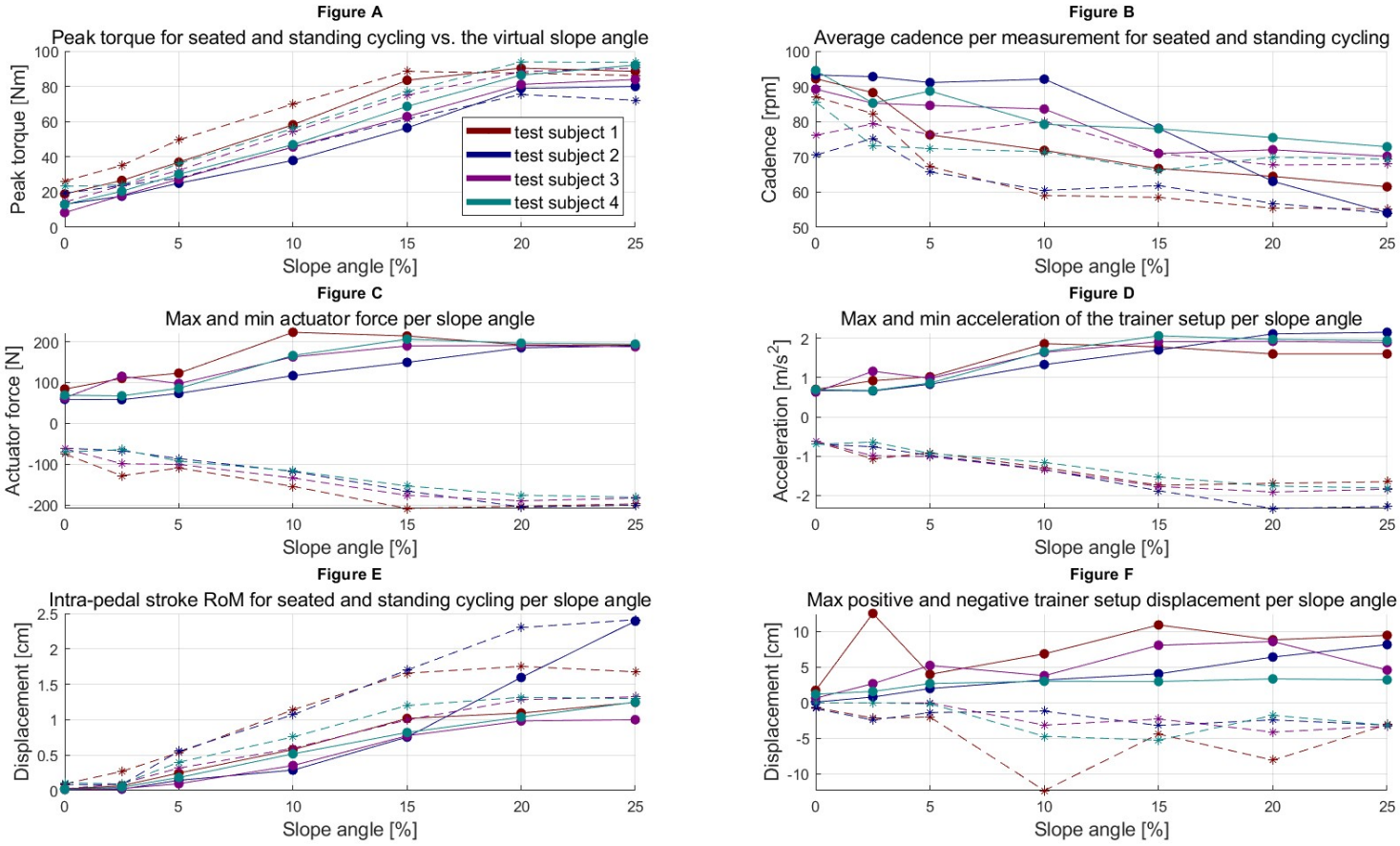

Figure (8.9) **Figure A** displays the peak torque for each test subject per slope angle, where the solid lines resemble the seated blocks and the dashed lines resemble the standing blocks of the data collection measurements. **Figure B** displays the cadence for each test subject per slope, where the solid lines resemble the seated blocks and the dashed lines resemble the standing blocks of the data collection measurements. **Figure C** displays the maximal positive and negative simulated actuator force for each slope angle for every test subject, where the solid lines resemble the seated blocks and the dashed lines resemble the standing blocks of the data collection measurements. **Figure D** displays the maximal and minimal simulated acceleration of the trainer setup per slope angle for each test subject. Where the solid lines resemble the positive acceleration and the dashed lines resemble the negative acceleration blocks of the data collection measurements. **Figure E** displays the simulated intra-pedal stroke range of motion per slope angle for each test subject, where the solid lines resemble the seated blocks and the dashed lines resemble the standing blocks of the data collection measurements. **Figure F** displays the maximal positive and negative simulated displacement of the trainer setup. Where the solid lines resemble the positive displacement and the dashed lines resemble the negative displacement blocks of the data collection measurements.

It stands out that the peak torque values are plateauing at around 90 Nm as the slope angles reach 20%. Whereas, the values are linearly increasing for the other measured virtual slope angles.

Overall the cadence with which the test subjects rode during the tests decreased as the resistance increased as a result of increasing the virtual slope angle. However, for some slope angles, the cadence was higher compared to the previous virtual incline. For seated cycling, the average cadence was higher compared to standing cycling.

The simulated magnitude actuator force increased as the resistance and therefore, the torque during the data collection tests increased. Just like the peak torque the values for the simulated maximal and minimal actuator force plateaued at 15% slope angle. Where the maximal actuator force is 223.11 N for test subject 1, who was the heaviest participant. The minimal actuator force was also simulated for test subject 1 at -208.52 N. Test subject 2, who is the lightest, accounts for the lowest simulated actuator force magnitudes ranging from 58.13 N to 189.58 N and -60.73 N to -204.88 N.

The trend of the simulated trainer setup acceleration and deceleration corresponds to the trend of the actuator force since it is a function of that force and the mass of the cyclist.

Intra-pedal stroke range of motion is the most important result of the simulated trainer setup motion as it is the small portion of motion that can be simulated indoors. From Figure 8.9 Figure E, it is clear that test subject 2 has the most intra-pedal stroke motion simulated. And it is the only test subject for which the intra-pedal stroke motion increased throughout all inclines for both seated and standing cycling. For the 3 other subjects, the intra-pedal stroke range of motion starts increasing less rapidly at an incline of 15%.

The final subplot F of Figure 8.9 displays the maximal positive and negative displacement of the simulated trainer setup. The maximal displacements stay within $\pm$ 20 cm of the initial trainer setup position, which is the requirement.

Note that for all tests subjects and slope angle simulations the settings of the simulator controller remained constant

When comparing the peak torque values around the rear wheel of the motion collection data conducted on the cycling treadmill to the peak torque during the tests on the static smart trainer, it can be observed that the measured peak torque on the treadmill increases more rapidly as the slope becomes steeper (Table 8.3). Note that the torque data is produced by the same test subject. Extrapolation of the treadmill torque to 20% end 25% slope angles will lead to an estimated torque of 120 Nm and 160 Nm, respectively.

Table (8.3) The peak torque around the rear wheel for treadmill cycling and static smart trainer cycling for various measured (virtual) inclines. Both peak torque values are measured during seated cycling.

Slope angle	0%	2.5%	5%	7.5%	10%	12.5%	15%	20%	25%
Treadmill peak torque [Nm]	11.35	20.90	32.62	44.44	57.07	71.39	87.50	-	-
Static smart trainer peak torque [Nm]	18.99	26.61	36.97	-	58.18	-	83.49	90.37	88.29

During the motion capture study on the cycling treadmill it became clear that the phase and period of the torque curve and the acceleration of the bicycle are the same (Figure A.7). However, for the results of the simulator controller simulations, the acceleration of the simulated trainer setup does correspond to that of the measured torque curve, as can be observed in Figure 8.10. The figure displays seated cycling on a 15% virtual slope by test subject 2. The same torque-acceleration relationship applies to the rest of the slope angles and the other test subjects as well.

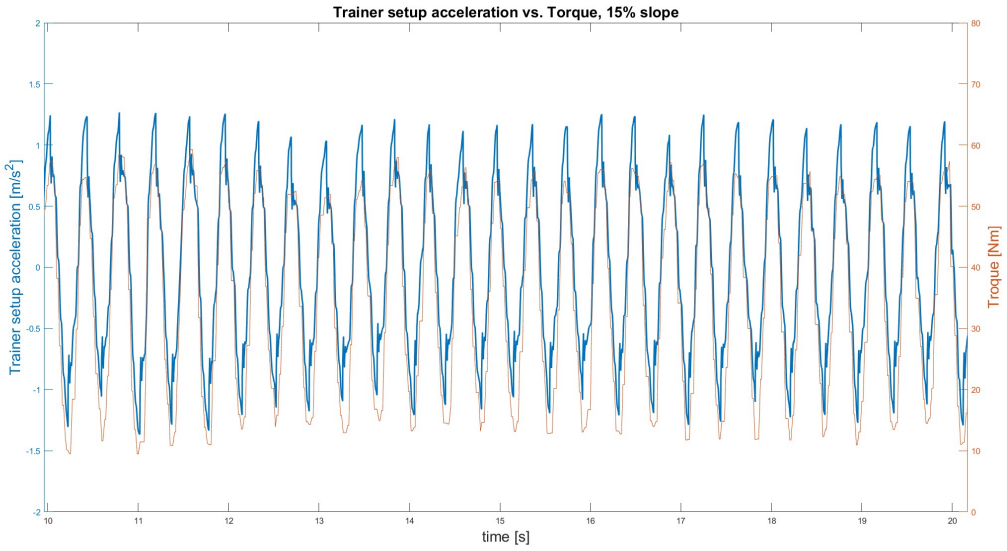

Figure (8.10) The virtual trainer setup acceleration and the measured torque curve for test subject 2 on a 15% virtual slope whilst cycling in the saddle.

Figure 8.11 displays the comparison between the motion capture data on the treadmill, the simulated motion based on the torque data from the motion capture test on the treadmill, and the simulations of with torque data acquired during tests on the static trainer. The intra-pedal stroke range of motion is the main performance metric of the simulator controller and, therefore, this metric is used to compare real-world treadmill cycling motion to the simulated motion of the trainer setup. The red line resembles the intra-pedal stroke range of motion of the motion tracking study on the treadmill. The blue line is a simulation of the trainer setup intra-pedal stroke range of motion with crank torque data acquired from the motion tracking study. The green line displays the average simulated intra-pedal stroke range of motion of all test subjects for torque data acquired on the static trainer.

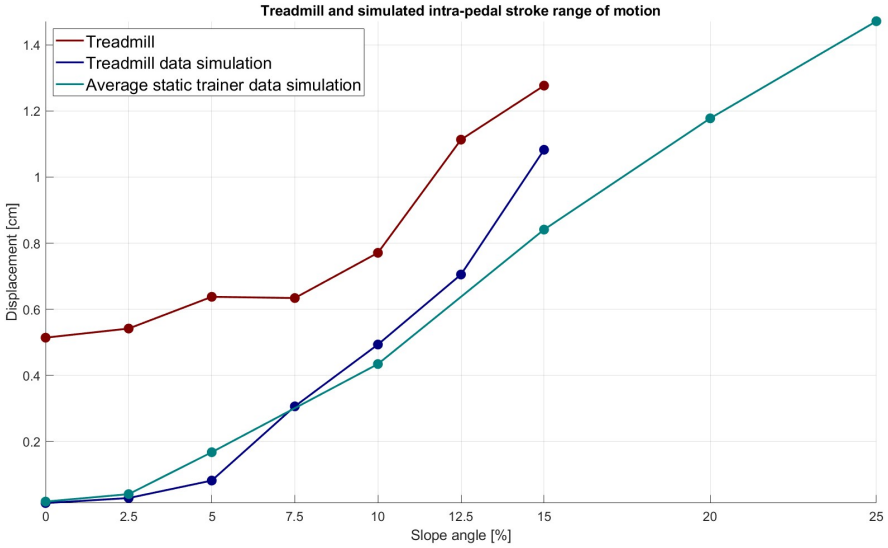

Figure (8.11) The intra-pedal stroke range of motion for a motion capture study on a cycling treadmill, for the simulation of the trainer setup based on treadmill torque data, and for the average simulated intra-pedal stroke motion of the trainer setup based static trainer torque data. Note that the intra-pedal stroke range of motion is the displacement measurement of the bicycle, whereas the other simulations simulate the motion of the cyclist, bicycle, and trainer as one body.

We observe that the motion captured intra-pedal stroke range of motion on the treadmill is greater than that of the simulated intra-pedal stroke range of motion for both the simulation with treadmill torque data and static trainer torque data. However, note that the motion-captured data was data from the bicycle position, whereas the simulated motion is that of the cyclist, bicycle, and trainer as one rigid body.

Another aspect that stands out is the increase in the intra-pedal stroke range of motion of the simulations is greater per step at shallower inclines compared to the motion capture data. Also when comparing the two simulated lines we observe that the static trainer simulation increases more rapidly at the two shallowest slopes.

However, we also observe that the intra-pedal stroke range of motion difference decreases with an increasing slope angle. Table 8.4 gives an overview of the difference between intra-pedal stroke range of motion per slope angle compared to treadmill cycling for both the simulations with treadmill acquired crank torque and static trainer torque.

Table (8.4) The difference between intra-pedal stroke range of motion between simulations with treadmill and static trainer acquired torque data, expressed as a percentage of treadmill intra-pedal stroke range of motion measured in treadmill cycling through a motion study.

Slope angle	0%	2.5%	5%	7.5%	10%	12.5%	15%
Treadmill motion vs. treadmill simulation	2.66%	5.34%	12.83%	48.32%	64.01%	63.34%	84.80%
Treadmill motion vs. static simulation	3.55%	7.52%	26.27%	-	56.34%	-	65.89%

Table 8.4 confirms what we see in Figure 9.1 and that is that the performance difference between the treadmill and the simulations decreases drastically.

In the coming chapter 9 the results will be discussed interpretation and the limitations of the results will be discussed in more detail to declare the results that stand out.

9 Discussion

9.1. Summary

The goal of this thesis is to design a simulator controller that can actively simulate realistic longitudinal outdoor cycling motion within a space-restricted indoor cycling setup. The simulator controller was designed and simulations of virtual indoor cycling trainer setups were performed to test the performance of the controller. The simulation results indicate that the simulator controller is able to simulate outdoor cycling motion within a restricted amount of space. Intra-pedal cycling motion is clearly present in the motion simulation of the trainer setup, which as well increased as the slope became steeper. Therefore, the cycling situation became harder. This simulator controller simulation behavior is expected and desirable since it resembles outdoor cycling dynamics.

The input signal for the controller is torque measured by the trainer during the data collection tests. After performing the motion tracking study it became clear that the acceleration of the bicycle has the same phase and period as the torque curve corresponding to it. The simulated acceleration of the trainer setup also has the same phase and period as its corresponding torque curve.

The trainer setup must not have any large displacement during the simulation as it could reach the end stops of the actuator in a physical setup. The displacement remains within $\pm$ 20 cm of its setpoint during the simulation which is a requirement as discussed in chapter 6. The minimization of the displacement without affecting the intra-pedal stroke range of motion is a direct result of the return-to-zero model that is implemented in the controller.

9.2. Interpretations

During the data collection experiments, the test subjects were asked to ride the virtual slopes as they would if it were outdoor cycling. This was asked to ensure the cycling was as realistic as possible for the given scenario. The test subjects succeeded in executing this task since the virtual velocity decreased as well as the cadence, whereas the delivered torque increased. This is assumed to also happen in outdoor cycling as the slope becomes steeper.

The input signal for the simulator controller was torque measured by the smart indoor cycling trainer, a Tacx Neo 2T. The measured torque is also the resistance the trainer produces to simulate virtual resistances, based on the virtual slope angle, virtual velocity, virtual rolling resistance, and the mass of the cyclist and bicycle. It stands out that the torque measured and, therefore, the torque applied to the cyclist plateaued for test subjects 1, 3, and 4 at around 90 Nm. This happens because the Tacx Neo 2T is not able to produce more than around 90 Nm of resistance and tests subjects 1, 3, and 4 produced more torque. The test subjects consequently all mentioned that it felt like the trainer slipped, which is a result of producing more torque than the trainer can produce as resistance.

The simulated longitudinal motion of the trainer setup does increase as cyclist-produced torque and slope increase while cadence decreases. This result matches the assumptions made in chapter 2. Where the thesis states that high cadence and velocity and low torque cycling lead to minimal difference longitudinal motion of the bicycle. Whereas low cadence and velocity and high torque lead to the most longitudinal change in bicycling motion.

We observe that for shallow slope simulations, where consequently virtual velocity is high due to relatively low virtual resistance, the intra-pedal stroke range of motion is the lowest for all test subjects. Whereas, if the virtual slope angle becomes steeper consequently the cadence and velocity decrease and torque increases, the intra-pedal stroke range of motion increases as expected. Only for test subject 2 the intra-pedal stroke range of motion kept increasing because she was the only test person who did not reach the torque limit of the trainer before the steepest virtual slope of 25%.

The maximal positive and negative simulated actuator force is increasing correspondingly to the peak torque values that the test subjects deliver. This result is expected as more peak torque must result in more intra-pedal stroke range of motion and therefore the actuator must apply more force to the trainer setup to achieve the increased motion.

As the actuator force becomes larger the simulated acceleration of the trainer setup must be larger as well since Newton's second law $F = m \cdot a$ applies. When observing the simulated acceleration results we see that acceleration is proportional to the actuator force. It can, therefore, be concluded that the motion simulation of the trainer setup was performed correctly.

The intra-pedal stroke range of motion is dependent on cadence and actuator force. The lower the cadence the more time the actuator has to drive the trainer setup, this agrees with the results of the thesis. Where the test subjects who adopted a lower cadence had more intra-pedal stroke motion for that simulated slope angle.

Since this thesis concerns longitudinal motion simulation in an indoor cycling trainer setup, it must be taken into account that the amount of motion must be limited. Therefore, a return-to-zero filter model was implemented into the actuator controller to ensure that no large displacements will occur. In the simulated result, the maximal displacement stays well within 15 cm of the initial trainer setup position. The return-to-zero model is based on a low-pass filter and a PD controller. The low-pass filter identifies the drift of the trainer setup without intra-pedal stroke motion. This drift value is then processed by the PD controller which reacts more aggressively to large drift and rapidly increasing drift. However, the low-pass filter has some amount of delay which introduces a delayed drift signal to the PD controller. Therefore, the position offset of the trainer setup is not directly pushed back to its setpoint. The aggressiveness of the controller may result in over- and undershoot which needs some time to settle. This happens when a sudden in- or decrease of cycling power occurs whilst cycling. This change in power causes acceleration or deceleration with corresponding drift.

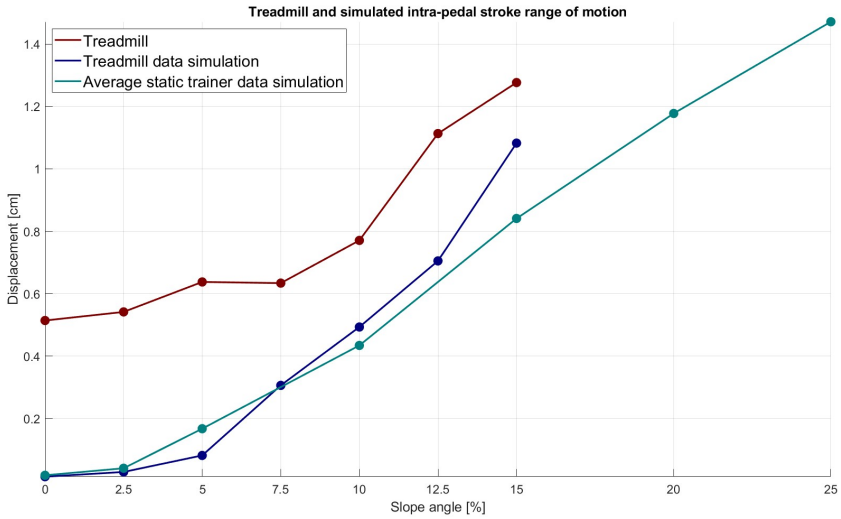

Figure (9.1) The intra-pedal stroke range of motion for a motion capture study on a cycling treadmill, for the simulation of the trainer setup based on treadmill torque data, and for the average simulated intra-pedal stroke motion of the trainer setup based static trainer torque data. Note that the intra-pedal stroke range of motion is the displacement measurement of the bicycle, whereas the other simulations simulate the motion of the cyclist, bicycle, and trainer as one body.

When comparing the intra-pedal stroke range of motion between the motion capture test on the cycling treadmill and the simulated intra-pedal stroke range of motion based on the treadmill and static trainer data, a few items stand out Figure 9.1. The motion on the treadmill does not increase constantly as

the slope angle does and the motion is greater than the simulated range of motion for every measured slope. Note that not all slopes were measured for both tests since the treadmill could not be set steeper than 15%.
The treadmill that was used is the Tacx Magnum as mentioned before. This is a smart cycling treadmill, meaning that the belt velocity automatically adjusts velocity if the cyclist reaches a certain distance to the rear or front end of the belt. If the cyclist comes too close to the front the belt will increase velocity to avoid the cyclist from hitting the front. If the cyclist comes too close to the rear end the belt will decrease velocity to avoid the cyclist from falling off. The belt speed control, unfortunately, interfered with the motion-tracking study which made it very difficult for the test subject to maintain a constant velocity. The test subject declared that on shallow slope angles, he was so focused on staying within the margins where the treadmill held constant speed, that the cycling did not feel realistic at all. While the slope angle of the treadmill increased it became easier for the test subject to maintain a constant speed. From a 5% incline and onward the test subject indicated that the cycling felt natural and that he did not have to focus as much to stay within the margins where belt speed remained constant.

While riding a cycling treadmill aerodynamic drag is absent which leads to less resistance whilst cycling at the same velocity compared to cycling on the static smart trainer which simulates all resistances, this declares the lower peak torque for cycling on the treadmill compared to the static trainer. Another factor that causes the difference in the intra-pedal stroke range of motion is the downscaling of the aerodynamic drag and the gravitational resistance forces by the controller. The actuator force is proportional to the size of the resistance forces, thus downscaling these leads to lower actuator force and consequently less motion.

However, we assume that the main reason why the treadmill intra-pedal stroke range of motion that is determined with the use of motion capture is larger is due to the fact that the treadmill intra-pedal stroke range of motion is that of the bicycle alone. Whereas the intra-pedal stroke range of motion for the simulated trainer setup is that of the cyclist, bicycle, and trainer a rigid body. We assume that the cyclist exerts forces on the bicycle which cause motion of the bicycle with respect to itself. That motion is seen back in the results of the motion capture study and declares the difference in intra-pedal stroke range of motion. Even if we run the crank torque data, acquired on the treadmill, through the simulator controller the intra-pedal stroke range of motion is lower. Since the motion is yet again calculated for the cyclist, bicycle, and trainer as one rigid body.

We also observed that the difference between the intra-pedal stroke range of motion between the treadmill motion data and the simulated motion, for both treadmill and static trainer-acquired, torque data, decreases as the slope angle increases. We assume that the difference at lower slope angles is less concerning since the motion is low and a difference will likely not make as much impact on the user experience. Whereas, the same percentage of difference on higher slope angles will affect the experience more since motion is greater.

9.3. Limitations

The data collection experiments to gather torque data as input signal for the controller simulation were performed on a Tacx Neo 2T smart indoor cycling trainer and on a Taxc Magnum cycling treadmill. The smart indoor cycling trainer is static which means that the bicycle has no longitudinal motion in it. However, this static torque data causes motion in the simulation of the trainer setup. It has been found that during nonstatic cycling the muscle patterns of the cyclist are different compared to static cycling [38]. Thus, a dynamic cycling torque signal might be different as well. It can therefore not be relied on that the static cycling input torque will lead to the same simulated motion as for dynamic cycling torque. The treadmill, however, does allow dynamic cycling but its belt speed is controlled which affects the torque the cyclist produced. Therefore, the torque data must be interpreted with caution.

The Tacx Neo 2T is a high-end indoor cycling trainer however, its resistance limit lies at around 90 Nm of torque. 3 of the 4 test subjects reached this limit during the measurements before the steepest slope. Consequently, the actuator force did not increase as the torque limit was reached. Therefore, it can not be concluded how the trainer set simulation will behave as torque is over 90 Nm.

The amount of test subjects was only 4 since the goal of the data collection was to determine how the controller behaves and not to measure data for machine learning or system identification purposes. However, since the torque limit was reached it would have been valuable to measure lightweight or untrained test subjects who can not produce 90 Nm of torque. In that way, a more complete understanding

of the controller's behavior can be established.

Actuator force is a function of the torque and the virtual resistance forces. Because the cyclist started at 0 initial virtual velocity, a virtual acceleration took place as the test subjects started pedaling during the measurements. This means that the sum of the average propulsion force and resistance force was not equal to zero. Therefore, the mean actuator force will not be equal to zero as well. If this actuator force would directly be used as actuator reference signal the trainer setup will accelerate to the average virtual velocity that was reached during the measurements. To avoid an average actuator force offset the calculated actuator force was detrended in Matlab before it was fed to the actuator controller part of the simulator controller. Thus, the simulator controller does not work real-time.

The low-pass filter that is used to identify the drift of the simulated trainer setup position has a delay as mentioned before. This delay causes the actuator controller also reacts delayed to drift, making position drift possible in the simulations. An optimized low-pass filter would lead to a faster reaction to the drift of the trainer setup.

In the controller, an actuator dynamics block was built to determine how the actuator would respond to the reference actuator force signal. No study on what actuator should be used for a physical setup has been conducted and therefore not the properties of a possible actuator. The actuator dynamics, therefore, only are a general suggestion and must be interpreted with caution.

The behavior simulator controller was simulated with torque data of real cyclists. However, the other forces a cyclist might apply to the bicycle are not taken into account when simulation the trainer setup motion. Every cyclist applied force differently to the bicycle and simulating it will result in a very generalized force and most likely will not suit the majority of the users. Therefore the cyclist can apply his or her own force to the bicycle to counteract the actuator force. Because the cyclist forces on the bicycle were left out of the simulation it is not possible to describe the results of simulations that include these forces.

During the motion capture experiments on the cycling treadmill, a marker was filmed in the longitudinal plane of the bicycle. The coordinates of the tracked marker resemble its position in that plane. However, the bicycle is able to translate over the lateral axis toward and away from the camera. This translation causes a change in the perspective of the marker, leading to the tracking software assessing the motion as more or less depending on the position. When determining the intra-pedal stroke range of motion of the marker an average value of the measurement was taken to mitigate the lateral translation effect. Nonetheless, the results must be interpreted with caution.

10

Conclusion and Recommendations

The goal of this thesis is to theoretically explore if it is able to translate outdoor cycling dynamics to an indoor cycling trainer setup, with torque as the only input. Hence, the to answer research question:

"What is the theoretical performance of a controller translating outdoor longitudinal cycling dynamics to an indoor simulator setup, with torque as the only input signal?"

Based on the simulations that were performed of the longitudinal actuated indoor cycling trainer setup, it can be concluded that it is able to translate outdoor longitudinal cycling dynamics to an indoor simulator setup, with torque as the only input.

Through Equation 5.7, the "Magic Equation", the simulator controller is able to translate the calculated longitudinal outdoor cycling forces to an actuator force that actuates the trainer setup leading to the desired longitudinal motion simulations.

The simulated longitudinal motion is as expected for the different cycling scenarios. Where the intra-pedal stroke range of motion is minimal in the low resistance simulated cycling situations and intra-pedal stroke range of motion is maximal during the high resistance simulated cycling situations. It can also be concluded that the simulator controller is able to act within the required space restriction of $\pm$ 20 cm. The maximal actuator force that was required to actuate the simulated trainer setup is determined to be 223.11 N. With this knowledge gained on the actuator, a study can be conducted to determine what actuator must be used in the building of a physical prototype.

The method of simulating the longitudinal cycling motion of the virtual trainer setup was done to gain a better understanding of the longitudinal cycling motion simulator controller without the need of building a physical setup. In that way, time could be used more effectively since building a physical concept is time-consuming and brings risks to it. Thus, for the restricted time the method of simulating the longitudinal motion of the trainer setup was the most suitable method.

Even though the results of this thesis satisfy the goal of assessing the theoretical performance of translating outdoor longitudinal cycling dynamic to an indoor cycling setup simulator, there are recommendations to make for future research. To get the best understanding of outdoor longitudinal bicycling dynamics field research must be performed. In that way, a true understanding of outdoor longitudinal bicycle motion can be gained. With that knowledge, the simulator controller can be evaluated more thoroughly. Field data does also eliminate the problem that an indoor cycling trainer reaches its resistance torque limit, which enables measuring test subjects who produce torque that exceed 90 Nm. Therefore, a larger spread of simulated cycling scenarios can be evaluated.

To simulate the actuator dynamics exactly an in-depth study on what actuator will be used in the physical concept will be implemented. If the properties of that actuator are known these can be added to the actuator dynamics block in the controller to evaluate how the simulator controller performs with that specific actuator.

Further research is needed to detrend the actuator force in real-time so that the simulator controller can completely function without intermediate processing of the data. Investigating a low-pass filter to

identify the actuator zero offsets might be a solution the achieve a pure real-time simulator controller.

Future research would consist of designing and building a physical trainer setup that is able to be controlled by the simulator controller actively and, therefore, simulates actual longitudinal motion based on the user's produced torque. It is the only way to investigate if longitudinal cycling motion feels realistic to the users. Because it will be an indoor setup with no actual velocity perception of what feels realistic and what is realistic might not be the same for cyclists using a physical setup. Therefore, user testing must be performed to identify if and what motion is experienced as similar to outdoor cycling.

The (smart) indoor cycling trainer industry does not include cycling trainers that are able the actively simulate longitudinal motion in a training setup. With the results of this thesis, it is proven that it is possible to translate outdoor longitudinal cycling dynamics to an indoor cycling setup, with torque as the only input. The performance of the simulator controller meets the requirements of holding the trainer setup within $\pm$ 20 cm of its setpoint, without affecting the intra-pedal stroke range of motion. When comparing the performance of the simulator controller to treadmill cycling we can conclude that the motion is similar when we keep the differences between the measurements in mind.

The knowledge gained with some additions can then be transferred to a physical model to build an indoor cycling trainer that does not exist yet and will most likely be an addition to the indoor cycling experience of cyclists.

Bibliography

[1] R. Buehler and J. Pucher, "Covid-19 impacts on cycling, 2019–2020," *Transport Reviews*, vol. 41, no. 4, pp. 393–400, 2021.

[2] M. Arkesteijn, J. Hopker, S. A. Jobson, and L. Passfield, "The effect of turbo trainer cycling on pedalling technique and cycling efficiency," *International journal of sports medicine*, vol. 34, no. 06, pp. 520–525, 2013.

[3] M. Chavarrias, J. Carlos-Vivas, D. Collado-Mateo, and J. Pérez-Gómez, "Health benefits of indoor cycling: A systematic review," *Medicina*, vol. 55, no. 8, p. 452, 2019.

[4] B. McIlroy, L. Passfield, H.-C. Holmberg, and B. Sperlich, "Virtual training of endurance cycling–a summary of strengths, weaknesses, opportunities and threats," *Frontiers in Sports and Active Living*, vol. 3, p. 631 101, 2021.

[5] D. Westmattelmann, J.-G. Grotenhermen, B. Stoffers, and G. Schewe, "Exploring the adoption of mixed-reality sport platforms: A qualitative study on zwift.," in *ECIS*, 2021.

[6] J. Freunek, S. Litzenberger, and F. Michel, "Saddle-pressure distribution and perceived comfort during inclined and upright cycling,"

[7] E. Bressel and B. J. Larson, "Bicycle seat designs and their effect on pelvic angle, trunk angle, and comfort," *Medicine and Science in Sports and Exercise*, vol. 35, no. 2, pp. 327–332, 2003.

[8] A. S. Larsen, F. G. Larsen, F. F. Sørensen, *et al.*, "The effect of saddle nose width and cutout on saddle pressure distribution and perceived discomfort in women during ergometer cycling," *Applied Ergonomics*, vol. 70, pp. 175–181, 2018.

[9] B. D. Lowe, S. M. Schrader, and M. J. Breitenstein, "Effect of bicycle saddle designs on the pressure to the perineum of the bicyclist," *Medicine and science in sports and exercise*, vol. 36, no. 6, pp. 1055–1062, 2004.

[10] J. P. Meijaard, J. M. Papadopoulos, A. Ruina, and A. L. Schwab, "Historical Review of Thoughts on Bicycle Self-Stability," en, p. 41, 2011.

[11] J. Meijaard, J. Papadopoulos, A. Ruina, and A. Schwab, "Linearized dynamics equations for the balance and steer of a bicycle: A benchmark and review," *Proceedings of The Royal Society A: Mathematical, Physical and Engineering Sciences*, vol. 463, pp. 1955–1982, Aug. 2007. DOI: 10.1098/rspa.2007.1857.

[12] A. L. Schwab and J. P. Meijaard, "A review on bicycle dynamics and rider control," *Vehicle system dynamics*, vol. 51, no. 7, pp. 1059–1090, 2013.

[13] R. Bini, P. Hume, J. Croft, and A. Kilding, "Pedal force effectiveness in cycling: A review of constraints and training effects," *Journal of Science and Cycling*, vol. 2, pp. 11–24, Jun. 2013.

[14] S. Dorel, J.-M. Drouet, A. Couturier, Y. Champoux, and F. Hug, "Changes of pedaling technique and muscle coordination during an exhaustive exercise," *Medicine+ Science in Sports+ Exercise*, vol. 41, no. 6, p. 1277, 2009.

[15] B. Fonda and N. Sarabon, "Biomechanics of cycling," *Sport Science Review*, vol. 19, no. 1-2, p. 187, 2010.

[16] W. Bertucci, F. Grappe, A. Girard, A. Betik, and J. D. Rouillon, "Effects on the crank torque profile when changing pedalling cadence in level ground and uphill road cycling," *Journal of biomechanics*, vol. 38, no. 5, pp. 1003–1010, 2005.

[17] B. J. Fregly, F. E. Zajac, and C. A. Dairaghi, "Bicycle drive system dynamics: Theory and experimental validation," *J. Biomech. Eng.*, vol. 122, no. 4, pp. 446–452, 2000.

[18] J. Baker, E. Brown, G. Hill, G. Phillips, R. Williams, and B. Davies, "Handgrip contribution to lactate production and leg power during high-intensity exercise.," *Medicine and Science in Sports and Exercise*, vol. 34, no. 6, pp. 1037–1040, 2002.

[19] C. Stone and M. L. Hull, “Rider/bicycle interaction loads during standing treadmill cycling,” *Journal of applied biomechanics*, vol. 9, no. 3, pp. 202–218, 1993.

[20] C. Stone and M. L. Hull, “The effect of rider weight on rider-induced loads during common cycling situations,” *Journal of biomechanics*, vol. 28, no. 4, pp. 365–375, 1995.

[21] M. B. Mellion, *Office sports medicine*. Hanley & Belfus, 1996.

[22] D. Sien, D. Jordi, M. Juwet, K. Shariatmadar, and M. Versteyhe, “Design and calibration of an instrumented seat post to measure sitting loads while cycling,” *Sensors*, vol. 20, no. 5, p. 1384, 2020.

[23] J. C. Martin, A. S. Gardner, M. Barras, and D. T. Martin, “Modeling sprint cycling using field-derived parameters and forward integration,” *Medicine and science in sports and exercise*, vol. 38, no. 3, p. 592, 2006.

[24] P. Debraux, F. Grappe, A. V. Manolova, and W. Bertucci, “Aerodynamic drag in cycling: Methods of assessment,” *Sports biomechanics*, vol. 10, no. 3, pp. 197–218, 2011.

[25] F. Grappe, R. Candau, B. Barbier, M. Hoffman, A. Belli, and J.-D. Rouillon, “Influence of tyre pressure and vertical load on coefficient of rolling resistance and simulated cycling performance,” *Ergonomics*, vol. 42, no. 10, pp. 1361–1371, 1999.

[26] G. Gibertini and D. Grassi, “Cycling aerodynamics,” in *Sport aerodynamics*, Springer, 2008, pp. 23–47.

[27] C. Baker and N. Brockie, “Wind tunnel tests to obtain train aerodynamic drag coefficients: Reynolds number and ground simulation effects,” *Journal of Wind Engineering and Industrial Aerodynamics*, vol. 38, no. 1, pp. 23–28, 1991.

[28] T. N. Crouch, D. Burton, Z. A. LaBry, and K. B. Blair, “Riding against the wind: A review of competition cycling aerodynamics,” *Sports Engineering*, vol. 20, no. 2, pp. 81–110, 2017.

[29] D. Fintelman, M. Sterling, H. Hemida, and F. Li, “The effect of time trial cycling position on physiological and aerodynamic variables,” *Journal of sports sciences*, vol. 33, no. 16, pp. 1730–1737, 2015.

[30] A. E. Jeukendrup and J. Martin, “Improving cycling performance,” *Sports Medicine*, vol. 31, no. 7, pp. 559–569, 2001.

[31] S. Berezvai, “Constitutive modelling of compressible solids including viscoelastic-viscoplastic effects,” Ph.D. dissertation, Budapest University of Technology and Economics (Hungary), 2020.

[32] C. Harnish, D. King, and T. Swensen, “Effect of cycling position on oxygen uptake and preferred cadence in trained cyclists during hill climbing at various power outputs,” *European journal of applied physiology*, vol. 99, no. 4, pp. 387–391, 2007.

[33] E. F. Hodson-Tole, O. M. Blake, and J. M. Wakeling, “During cycling what limits maximum mechanical power output at cadences above 120 rpm?” *Medicine and Science in Sports and Exercise*, vol. 52, no. 1, p. 214, 2020.

[34] C. R. Abbiss, J. J. Peiffer, and P. B. Laursen, “Optimal cadence selection during cycling,” *International SportMed Journal*, vol. 10, no. 1, pp. 1–15, 2009.

[35] C. Abbiss, J. Peiffer, and P. Laursen, “Optimal cadence selection during cycling,” *ECU Publications*, vol. 10, Mar. 2009.

[36] J. Brisswalter, C. Hausswirth, D. Smith, F. Vercruyssen, and J. Vallier, “Energetically optimal cadence vs. freely-chosen cadence during cycling: Effect of exercise duration,” *International journal of sports medicine*, vol. 21, no. 01, pp. 60–64, 2000.

[37] T. Defraeye, B. Blocken, E. Koninckx, P. Hespel, and J. Carmeliet, “Aerodynamic study of different cyclist positions: Cfd analysis and full-scale wind-tunnel tests,” *Journal of biomechanics*, vol. 43, no. 7, pp. 1262–1268, 2010.

[38] M. Arkesteijn, S. Jobson, J. Hopker, and L. Passfield, “The Effect of Cycling Intensity on Cycling Economy During Seated and Standing Cycling,” en_US, *International Journal of Sports Physiology and Performance*, vol. 11, no. 7, pp. 907–912, Oct. 2016, Publisher: Human Kinetics, Inc. Section: International Journal of Sports Physiology and Performance, ISSN: 1555-0273, 1555-0265. DOI: 10.1123/ijspp.2015-0441. [Online]. Available: https://journals.humankinetics.com/view/journals/ijspp/11/7/article-p907.xml (visited on 04/11/2022).

Appendix A - Treadmill Bicycle Acceleration

This Appendix A displays all the plots for the marker acceleration produced during the motion capture study that is discussed in chapter 3.

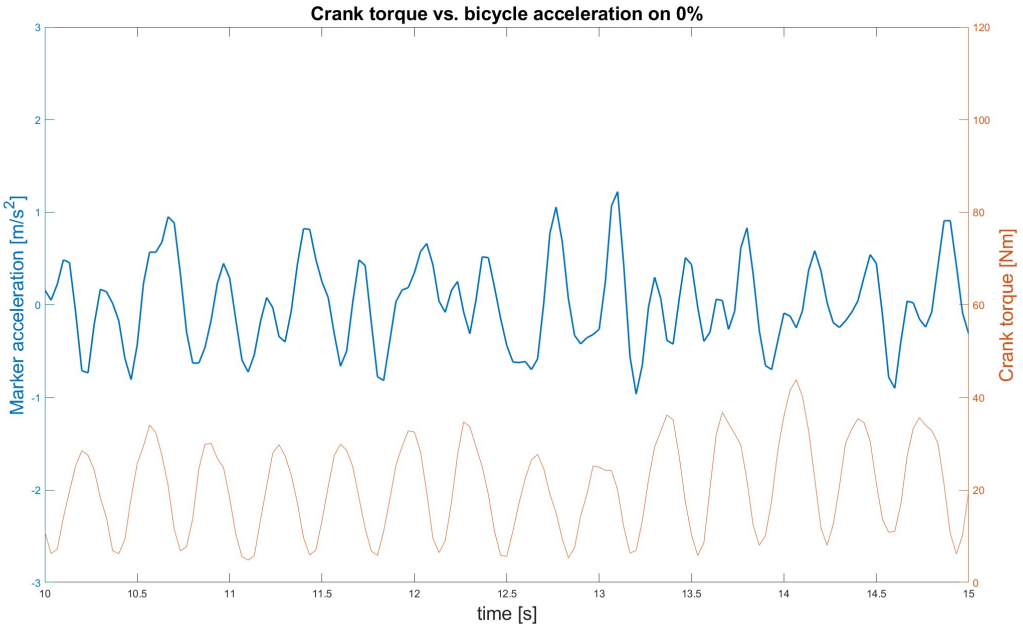

Figure (A.1) Bicycle rear wheel axis marker acceleration and the corresponding crank arm torque for 0% incline cycling treadmill riding.

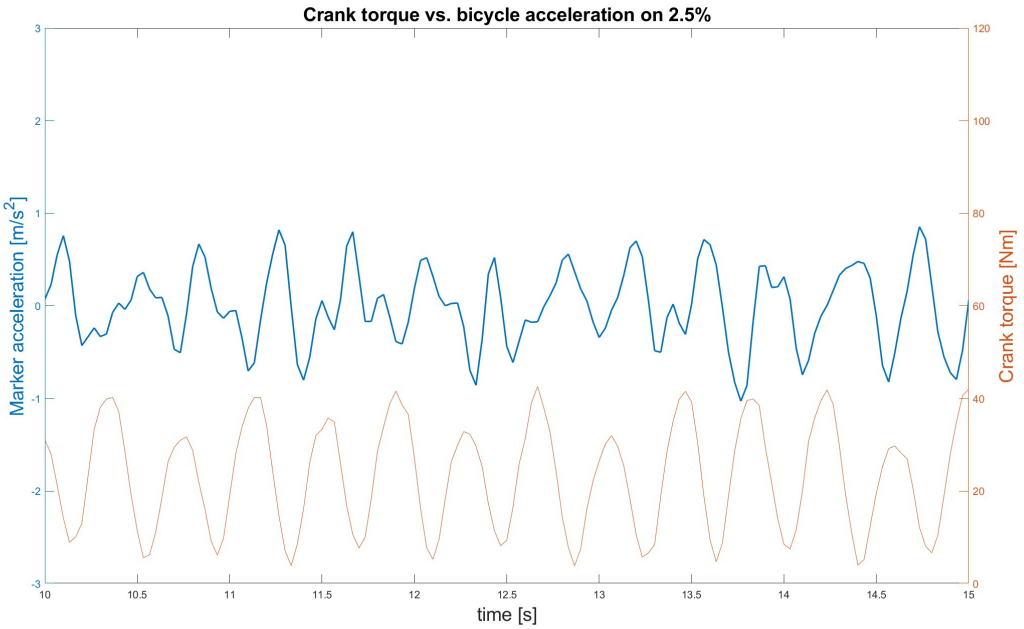

Figure (A.2) Bicycle rear wheel axis marker acceleration and the corresponding crank arm torque for 2.5% incline cycling treadmill riding.

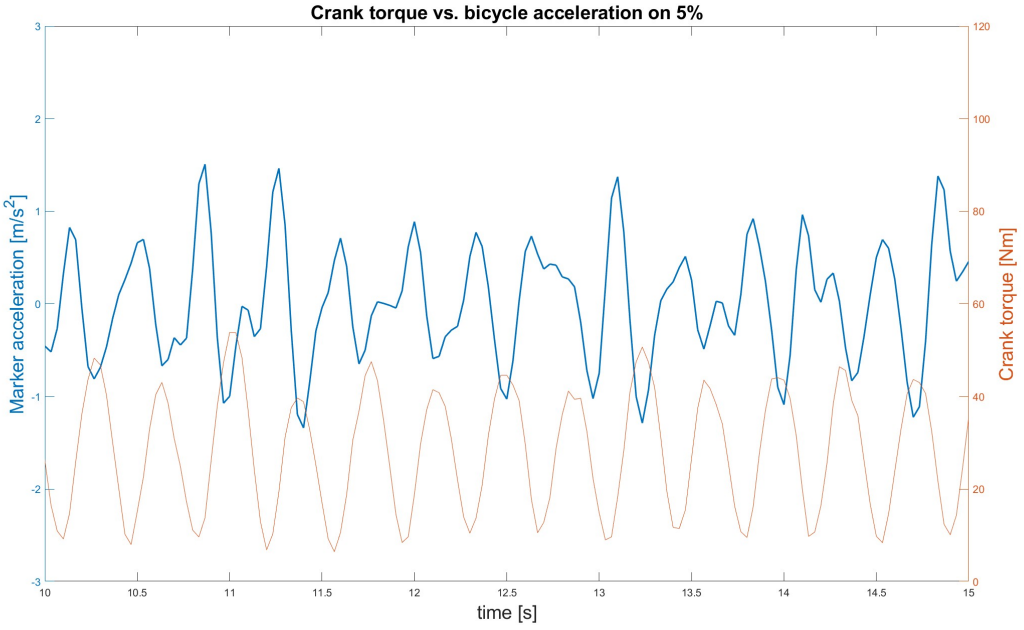

Figure (A.3) Bicycle rear wheel axis marker acceleration and the corresponding crank arm torque for 5% incline cycling treadmill riding.

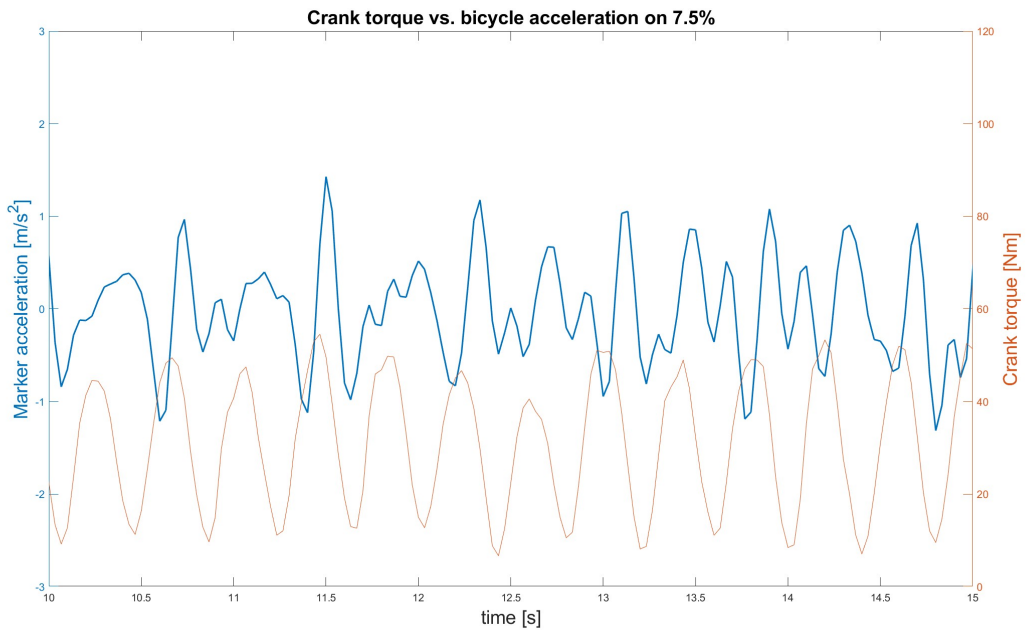

Figure (A.4) Bicycle rear wheel axis marker acceleration and the corresponding crank arm torque for 7.5% incline cycling treadmill riding.

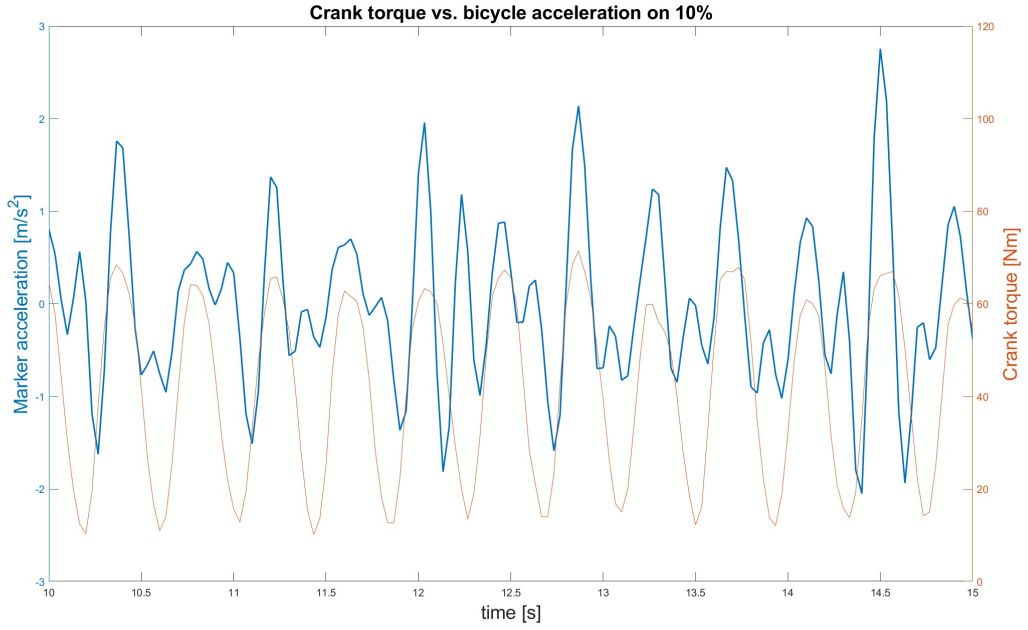

Figure (A.5) Bicycle rear wheel axis marker acceleration and the corresponding crank arm torque for 10% incline cycling treadmill riding.

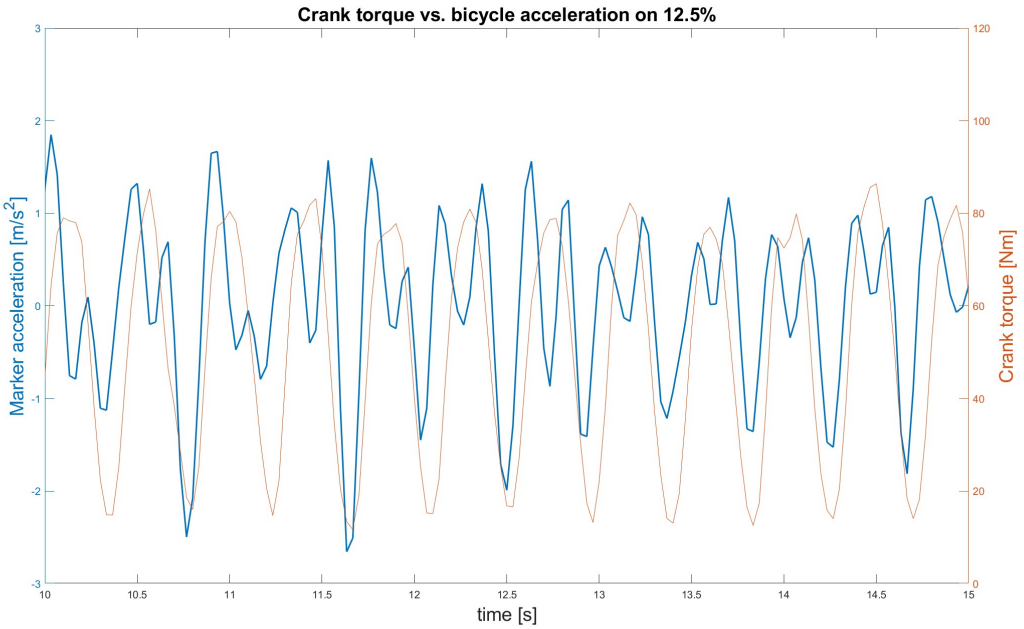

Figure (A.6) Bicycle rear wheel axis marker acceleration and the corresponding crank arm torque for 12.5% incline cycling treadmill riding.

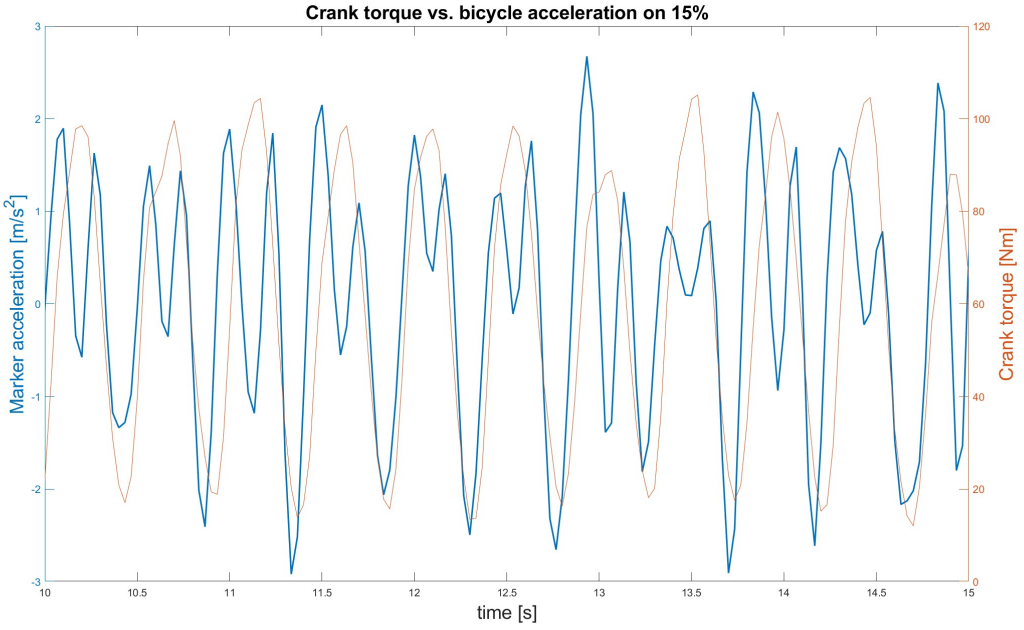

Figure (A.7) Bicycle rear wheel axis marker acceleration and the corresponding crank arm torque for 15% incline cycling treadmill riding.

B

Appendix B - Trainer Rolling Resistance Determination

To account for rolling resistance in the ”Magic Equation” (Equation 5.7) an experiment was performed to determine the rolling resistance coefficient (C_{rr}) of a rolling trainer.

B.1. Equipment

1. A Tacx Neo 2T (Tacx, Oegstgeest, Netherlands).
2. Tacx Motion plates (Tacx, Oegstgeest, Netherlands).
3. A PCE Instruments PCE-HS 50N digital force meter (PCE Instruments, Enschede, Netherlands).

Tacx Motion Plates (Figure 1.3) are an accessory to allow passive longitudinal motion in a Tacx Neo 2T. The Motion Plates, are made of two plates that are on top of each other with wheels in between so that they can slide over each other. The Taxc Neo 2T and Motion Plates weigh 21.5 kg combined.

B.2. Protocol

1. The Tacx Neo 2T was placed on the motion plates.
2. The force meter was attached to the Tacx Neo 2T through the carbine which was on the force meter.
3. The force meter was then pulled to the moment motion was initiated and the force at that moment was read from the display of the force meter.

B.3. Result

We measured that the rolling resistance of the trainer on wheels was 7 N. To determine its C_{rr} the rolling resistance force must be divided by the normal force of the trainer and Motion Plates which resulted in:

$$Crr = \frac{F_{rr}}{F_N} = \frac{7}{21.5 \cdot 9.81} = 0.033 \tag{B.1}$$

The calculated C_{rr} value can then be used to determine the rolling resistance of the rolling indoor trainer in order to complete the ”Magic Equation”.